

Supporting information

Enabling highly-efficient and stable potassium-ion storage by exposing atomic-dispersed super-coordinated antimony $O_2Sb_1N_4$ sites on N-doped carbon nanosheets

Bensheng Xiao^{a,#}, Zhefei Sun^{a,#}, Hehe Zhang^a, Ying Wu^b, Ji Li^{d,e}, Jiang Cui^f, Jiajia Han^{a,*}, Miao Li^a, Hongfei Zheng^a, Jiamin Chen^a, Mengting Cai^{a,i}, Chengzhi Ke^a, Xuefeng Wang^g, Haodong Liu^h, Zheng Jiang^{d,e}, Shilin Zhang^c, Dong-Liang Peng^a, Zaiping Guo^{c,*}, Qiaobao Zhang^{a,*}

^a State Key Laboratory of Physical Chemistry of Solid Surfaces, College of Materials, Xiamen University, Xiamen 361005, Fujian, China

^b School of Materials and Energy, Lanzhou University, Lanzhou 730000, China

^c School of Chemical Engineering, The University of Adelaide, Adelaide, 5005 Australia

^d Shanghai Institute of Applied Physics, Chinese Academy of Science, Shanghai 201210, China

^e Shanghai Synchrotron Radiation Facility, Zhangjiang Lab, Shanghai Advanced Research Institute, Chinese Academy of Science, Shanghai 201210, China

^f Department of Materials Science and Engineering, Clemson University, Clemson, SC 29634, USA

^g Beijing National Laboratory for Condensed Matter Physics, Institute of Physics, Chinese Academy of Sciences, Beijing, 100190 P. R. China

^h Chemical Engineering, UC San Diego, La Jolla, CA 92093, USA

ⁱ College of Chemistry and Chemical Engineering, Hubei University, Wuhan 430062, China

*Corresponding Authors:

Jiajia Han, E-mail: jiajiahan@xmu.edu.cn

Zaiping Guo, E-mail: zaiping.guo@adelaide.edu.au

Qiaobao Zhang, E-mail: zhangqiaobao@xmu.edu.cn

These authors contributed equally to this work.

1. Experimental detail

Preparation of O-Sb-N SA@NCs:

The O-Sb-N SAs/NC samples were mainly synthesized by coordination-intercalation assisted strategy under the one-step carbonization process. First, antimony chloride (SbCl_3) with different content (0.15, 0.3, and 0.6 g), 6.0 g dicyanamide (DCDA), and 0.6 g homophenyltrionic acid dissolved in 30 ml ethanol solution, stirring magnetically for 36 h at room temperature to form a homogenous solution. Second, the above homogenous solution was dried in an oven at 80 °C for one night. Finally, the obtained dried mixture was ground into a powder and placed into the tubular furnace heated for 2 h at 800 °C (heating speed of 5 °C min^{-1}) under an N_2 atmosphere to achieve the target materials, which were marked as O-Sb-N SA@NC₁, O-Sb-N SA@NC₂, O-Sb-N SA@NC₃, respectively.

Preparation of bare NC

The difference in the preparation of NC and Sb O-Sb-N SA@NC is that without the introduction of any Sb sources and other synthesis processes stay the same.

Preparation of Sb NP@NC

200 mg above solid powders of bare-NC and 50 mg SbCl_3 were dissolved in 30 ml ethanol and stirred continuously for 2h. Moreover, then dried in an oven at 80 °C for one night. The as-obtained solid powders were subsequently annealed at 400 °C under the H_2/Ar mixed atmosphere for 1 h with a ramping rate of 2 °C /min to achieve Sb NP@NC.

Material Characterization

Ingredient information of bare-NC, O-Sb-N SA@NC₁, O-Sb-N SA@NC₂, O-Sb-N SA@NC₃, and Sb NP@NC were analyzed by XRD (Bruker-axs X-ray diffractometer equipped with Cu-K α radiation). The morphology and structure information of five samples were investigated by Scanning Electron Microscope (Zeiss SIGMA) and Transmission Electron Microscope (FEI Talos F200s). XPS (Thermo Scientific K-Alpha) was used to characterize the chemical states. Specific surface areas and pore sizes were tested by N adsorption and desorption using a Micromeritics APSP 2460. Raman spectra were collected on a Renishaw spectrometer at 532 nm using DXR 2Xi. Cryogenic-transmission electron microscopy (Cryo-TEM) characterizations of the cycled electrode were carried out using a JEOL JEM-F200 microscope under cryogenic temperatures (-180°C) at 200 kV. The cycled electrode was rinsed by DME slightly two times and dried in the vacuum mini-chamber of the glove box. The sample for Cryo-TEM characterizations was scraped from the cycled electrode sheets, and then dispersed on the TEM grids. It was loaded on the Cryo-TEM holder (Fischione 2550) in the glove box and transferred into JEOL JEM-F200 microscope without air exposure with the help of a sealing design. Liquid nitrogen was added to the Cryo-TEM holder and the sample temperature dropped and stabilized at -180°C.

***In situ* Raman Characterization**

Raman measurements were performed on a TriVista CRS557 Raman microscope (Princeton Instruments, UK) using a holographic grating of 1,800 g/mm. The excitation laser (532 nm) was focused through a 50×objective. The laser power was 234 μW, and the acquisition time was 10 s seconds 3 times. *In situ* Raman cell boxes were purchased from Tianjin, Aida Hengsheng. The galvanostatic charge/discharge process was tested by using a NEWARE CT-3008W tester between 0.01 and 3 V. The atlas was collected when the voltage changed by 0.1 V. All Raman spectra were normalized and smoothed.

***In situ* TEM Observations**

A typical nanoscale electrochemical open cell was built inside an FEI Talos-F200s TEM with a 200 kV acceleration voltage using Nanofactory TEM-STM specimen holder. O-Sb-N SA@NC₂ were attached on a half a Mo ring for use as the working electrode. A copper tip loaded with a small amount of potassium is used as the counter electrode, and the naturally occurring K₂O on the surface of the K metal acts as an electrolyte. When the K₂O/K electrode was moved into contact with the O-Sb-N SA@NC, a bias (±3V) driving force was applied to the copper tip, and the potassization/depotassization behavior immediately began.

Electrochemical Characterizations

The working electrodes were prepared by mixing the active material, conductivity agent (Super P), and CMC with a weight ratio of 80:10:10 and coated uniformly on Cu foil and dried in a vacuum oven at 60 °C overnight. The mass loadings of the active materials were measured to be 1.5–1.8 mg cm⁻². The coin-type cells (2016) were assembled in an Ar-filled glove box (Mikrouna). A potassium metal was used as a counter electrode, glass fiber (GF/D) was used as the separator, and the electrolyte was a 1 M KFSI solution dissolved in dimethyl ether (DME). Galvanostatic charge/discharge measurements were tested using a NEWARE CT-3008W tester between 0.01 and 3 V at 25 °C under different current densities. CV measurements and electrochemical impedance spectroscopy (EIS) were conducted on an electrochemical workstation (Chenhua, Shanghai, China) in the voltage range of 0.01–3.0 V (vs. K/K⁺). For the full cell, KFeHCF was selected as the cathode. The KFeHCF cathode was prepared by mixing 80 % KFeHCF (K_{1.92}Fe [Fe (CN)₆]_{0.94}·0.5H₂O), 10 % acetylene black, and 10 % PVDF dissolved in an appropriate amount of NMP to form the slurry. Prior to assembling the full batteries, the anode material was cycled in a half cell to realize activation. The electrolyte was 1 M KFSI in DME. The cathode material was 20 % more in excess of capacity than the anode material and the mass loadings of the cathode material is measured to be about 8.22 mg. The cut-off voltage window for the full cell was between 1.0 and 3.8 V. The capacity of the full cell was calculated based on the mass of the active material in the anode.

DFT calculations

All spin-polarized calculations were conducted by using density functional theory (DFT) as implemented in the Vienna *Ab initio* Simulation Package (VASP)¹⁻³, with the

projector-augmented wave method (PAW)⁴ describing the ion-electron interaction. The valence electrons were taken into account using a plane wave basis set with a kinetic energy cut-off of 600 eV, which guarantees that the total energy was converged to 1 meV per atom. The generalized gradient approximation (GGA) with Perdew–Burke–Ernzerhof (PBE)^{5,6} functionals was used to express the interacting electron exchange–correlation energy, with an electronic convergence criterion of 10^{-6} eV and an ionic convergence criterion of 10^{-2} eV \AA^{-1} . The van der Waals interaction was considered by the empirical correction of Grimme’s scheme (DFT-D3)⁶. The $5 \times 5 \times 1$ supercell of graphene facet with a vacuum gap of 15 \AA was taken as the substrate model. The Brillouin zone was sampled by Gamma centered $3 \times 3 \times 1$ Monkhorst-Pack grid for structural optimizations and a $4 \times 4 \times 1$ Monkhorst-Pack grid for static calculation. Minimum energy pathways were investigated using the climbing image nudged elastic band method (CI-NEB)⁷. The path threshold for CI-NEB calculations was set to 0.02 eV \AA^{-1} , and the insertion points were determined by the displacement of the diffusion atom.

The adsorption energy of K^+ ($E_{\text{ads-K}}$) is defined as:

$$E_{\text{ads-K}} = E_{\text{total}} - E_{\text{substrate}} - E_{\text{K}} \quad \text{Equation S1}$$

where E_{total} , $E_{\text{substrate}}$, and E_{K} denote the total energy of substrate with one K^+ , substrate, and one K^+ , respectively.

The formation energy (E_f) is expressed as:

$$E_f = E_{\text{total}}(n) - E_{\text{total}}(n-1) - E_{\text{K}} \quad \text{Equation S2}$$

where $E_{\text{total}}(n)$ and $E_{\text{total}}(n-1)$ denote the total energy of substrate with n K^+ and $n-1$ K^+ , respectively.

The deintercalation energy (E_{de}) is expressed as:

$$E_{\text{de}} = E_{\text{total}}(n-1) + E_{\text{K}} - E_{\text{total}}(n)$$

Finite element analysis (FEA)

FEA was employed to simulate the electrochemo-mechanical stress for the potassiation of Sb sphere and Sb sphere/C. The dimension and geometry of the models were taken based on the experimental characterizations. The three dimensional models were meshed with tetrahedrons due to the irregularity of the geometries and boundaries of the Sb sphere/C, and the density of the meshes were determined by a convergence test. The electrochemo-mechanical behavior was modeled by the Fick’s law of diffusion and a linear correlation between the potassium concentration and the potassiation-induced strain according to the previous study⁸. We treat both the original Sb sphere/C and the potassiated product as elastic materials, and their deformation upon potassiation follows the classic Hooke’s law in three dimensions. Finally, a non-linear concentration-dependent diffusivity is used to model the alloying reaction for Sb containing species. The calculated stresses are 1st principal stresses normal to the plane in which the shear stress is zero.

Figure S1

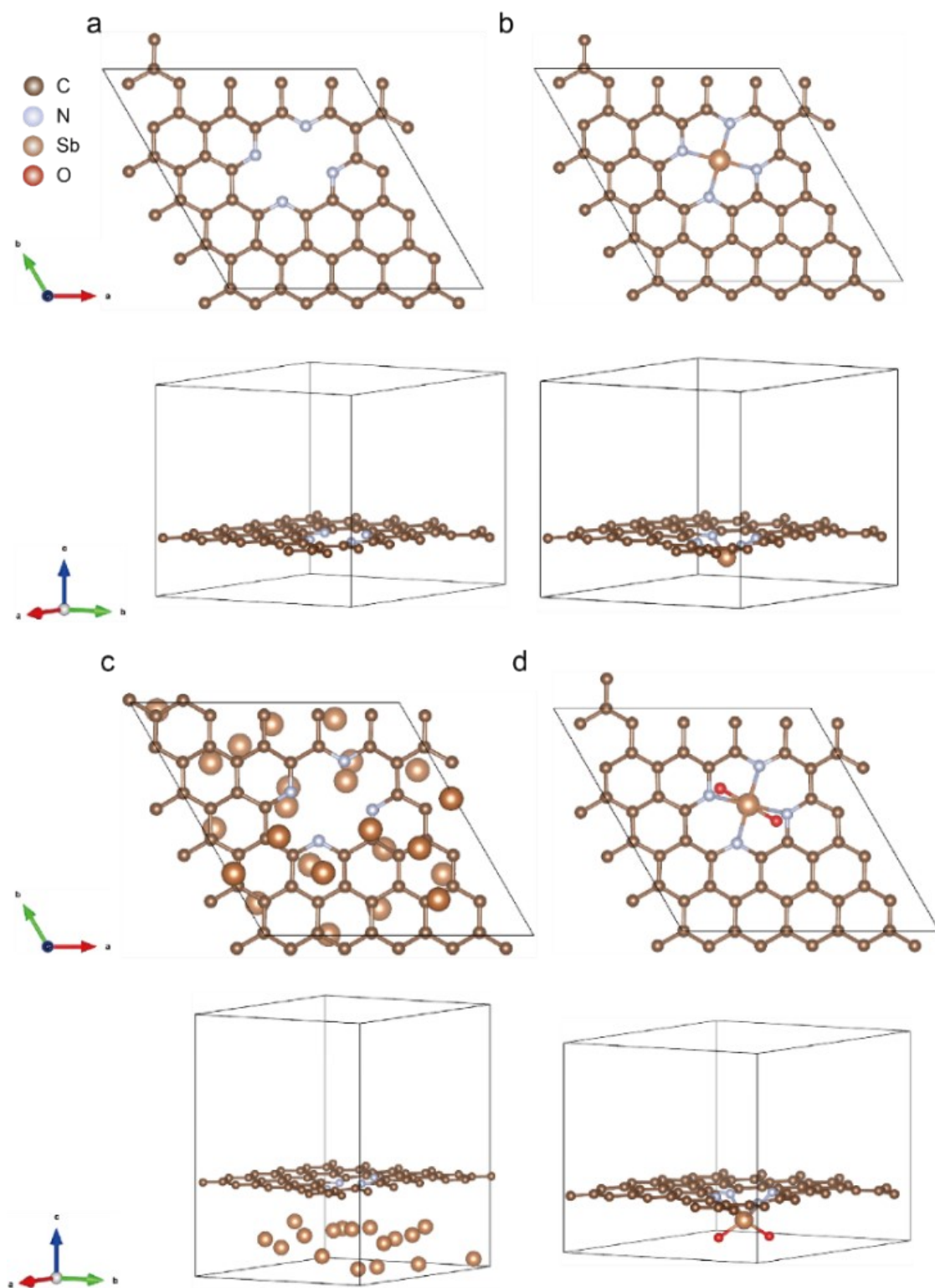


Figure S1. (a, b) Top and side views of the atomic structure of (a) bare NC, (b) Sb-N SA@NC, (c) Sb NP@NC, and (d) O-Sb-N SA@NC, respectively.

DFT calculations show that the defect formation energy of hexagon C ring is significantly lower than that of pentagon C ring, with a smaller C atomic spacing near the defect (Figure S2). These results indicate that defects of hexagon C ring should form more readily than that of pentagon C ring under the same conditions. The pentagon C ring, together with the distorted heptagon C ring, imparts a higher activity to the defect, resulting in the formation energy of the pyrrolic N having a greater negative value than that of the pyridinic N and a larger adsorption energy for Sb (Figure S3a and b). The difference in configuration between the pyrrolic 4N-Sb and the pyridinic 4N-Sb occurred when the defective C was adsorbing K ions or the Sb was in an oxidized state. As shown in Figure S3c, the adsorption of K ions on the surface of Sb-N SA@NC resulted in a structural transformation from 4N-Sb to 2N-Sb. This change can be confirmed by the charge density difference between the two structures, as illustrated in Figure S3e. Moreover, the 4N-Sb-2O configuration in O-Sb-N SA@NC was unstable in pyrrolic defective C and spontaneously transformed into 2N-Sb-2O (Figure S3d and Figure S3f).

Figure S2

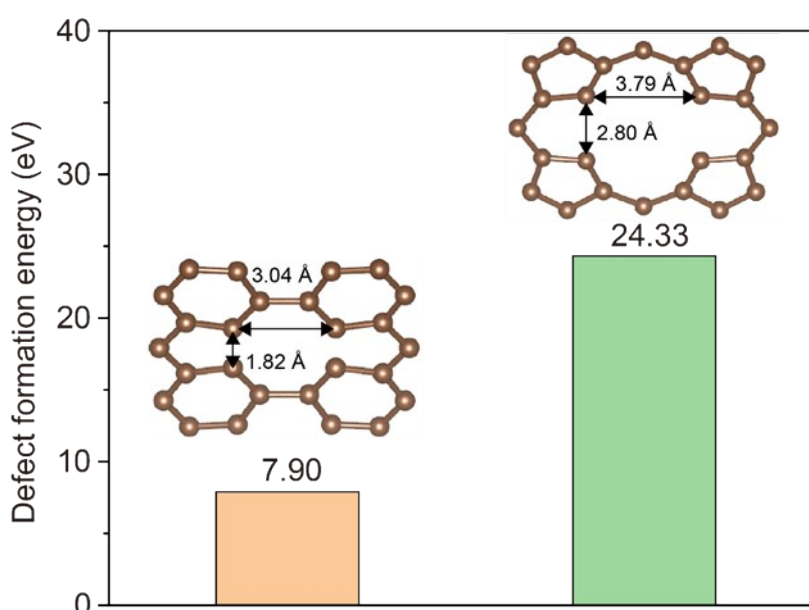


Figure S2. Defect formation energy of pentagon C ring and hexagon C ring, respectively.

Figure S3

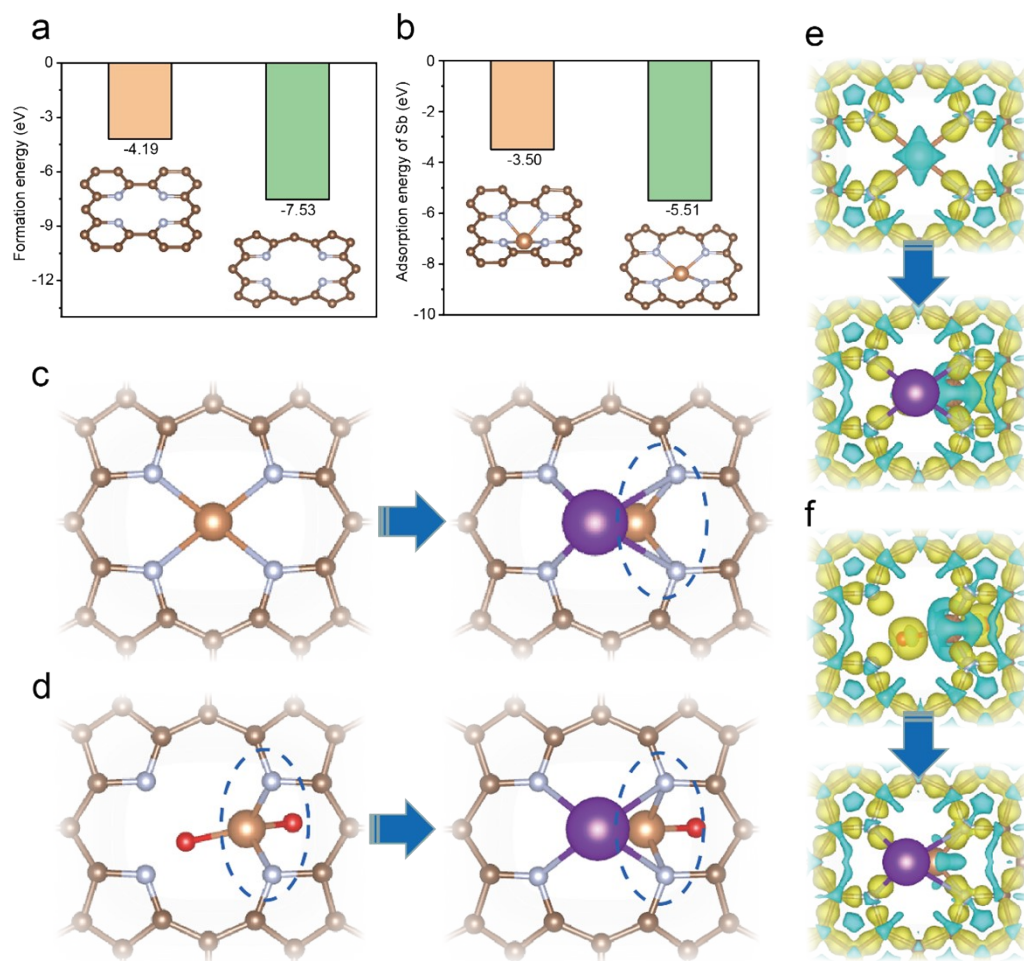


Figure S3. (a) Formation energy of pyrrolic 4N and pyridinic 4N, respectively. (b) Adsorption energy of Sb on pyrrolic 4N and pyridinic 4N, respectively. (c) Stable atomic configurations of pyrrolic Sb-N SA@NC and pyrrolic O-Sb-N SA@NC as well as their K-adsorbed states. (e-f) Charge density difference (CCD) of the corresponding configurations in (c) and (d), respectively.

Figure S4

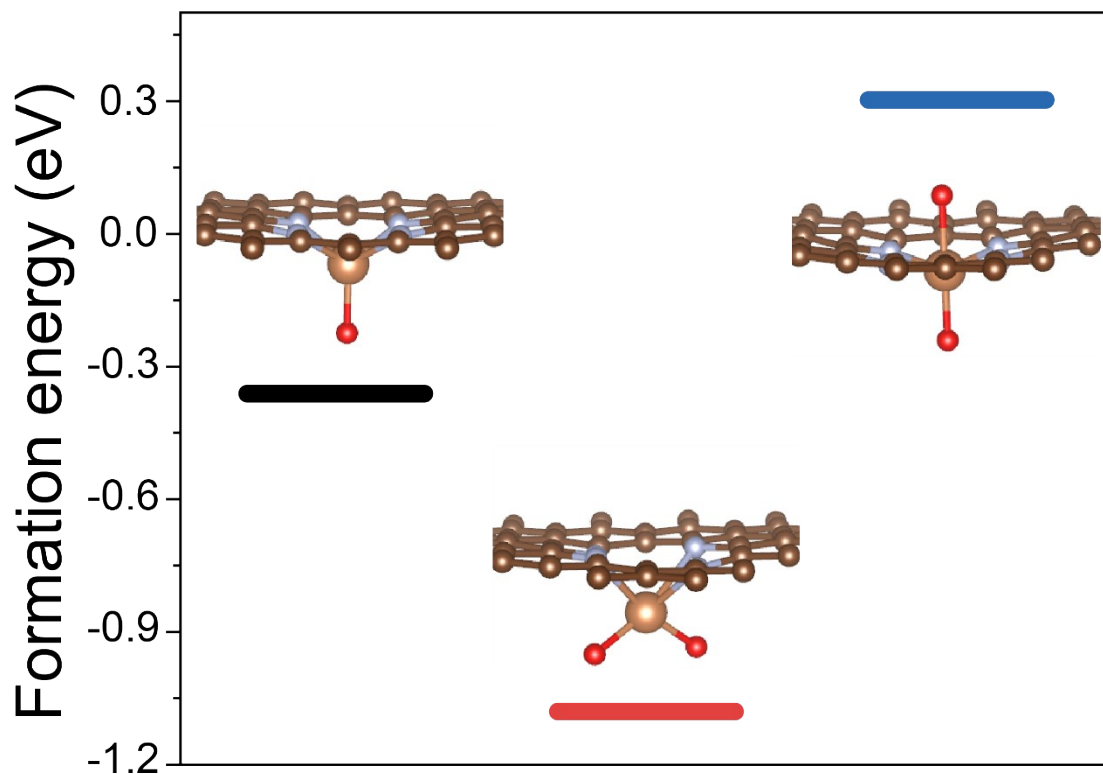


Figure S4. Formation energy of Sb-N SA@NC with different adsorbed state of oxygen atoms. The atomic structure of O-Sb-N SA@NC was determined according to the formation energy of Sb-N SA@NC, where the O-Sb-N SA@NC with the low formation energy at around -1.2 eV was chosen.

Figure S5

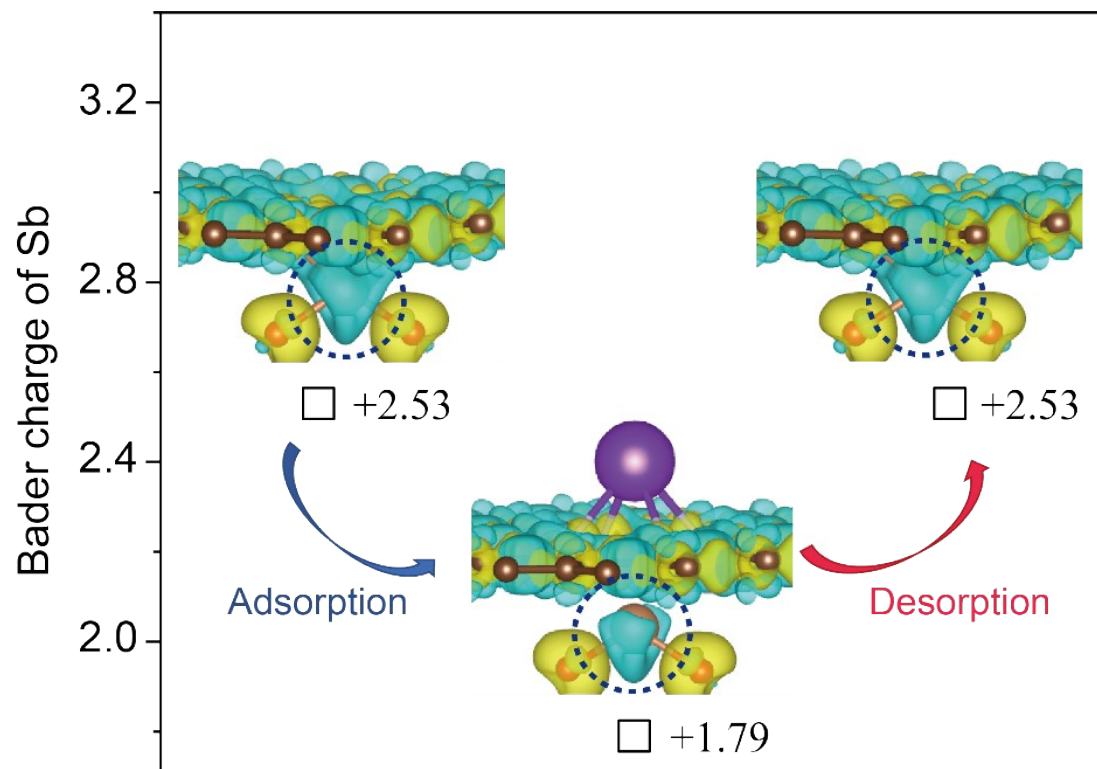


Figure S5. Bader charge of Sb atom during adsorption and desorption of single K^+ . The inset shows the charge density difference in each step, where the dotted circle signals the spatial position of the Sb atom.

Figure S6

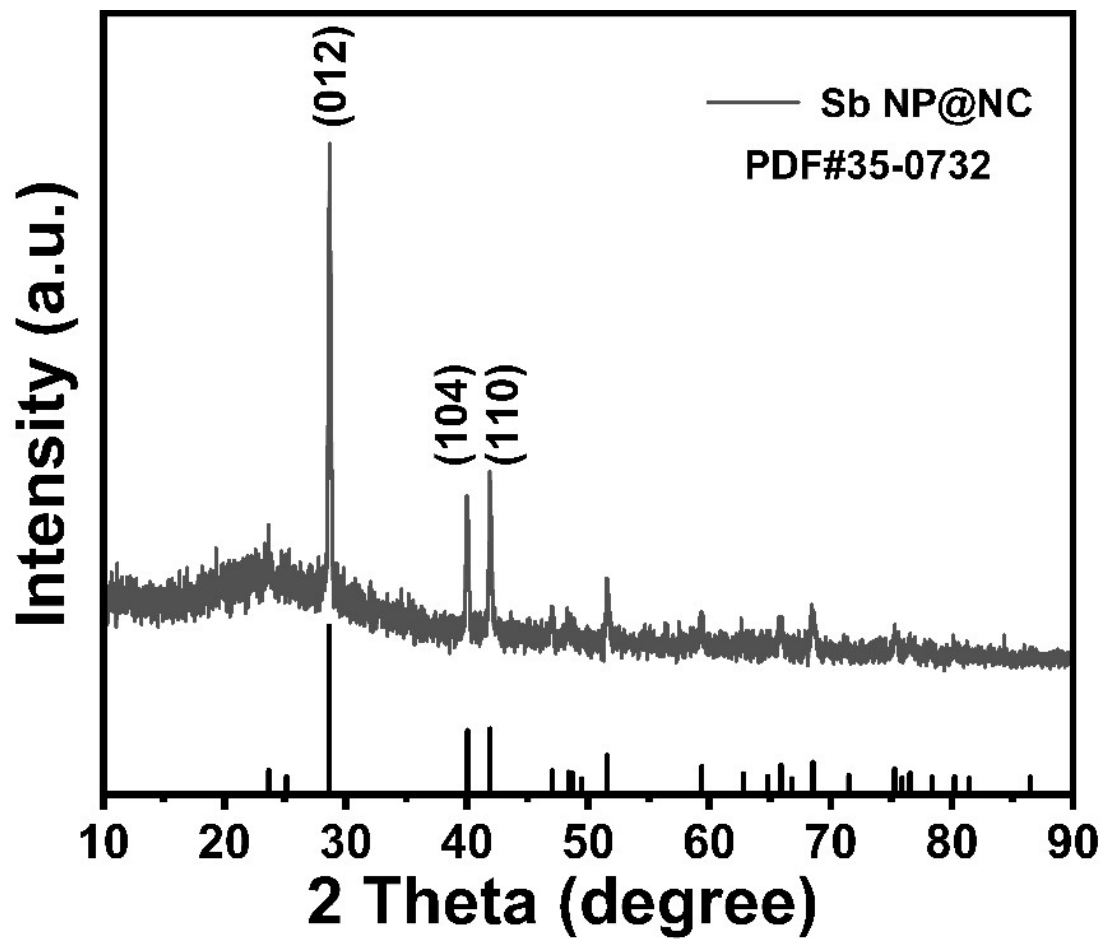


Figure S6. XRD pattern of Sb NP@NC sample.

Figure S7

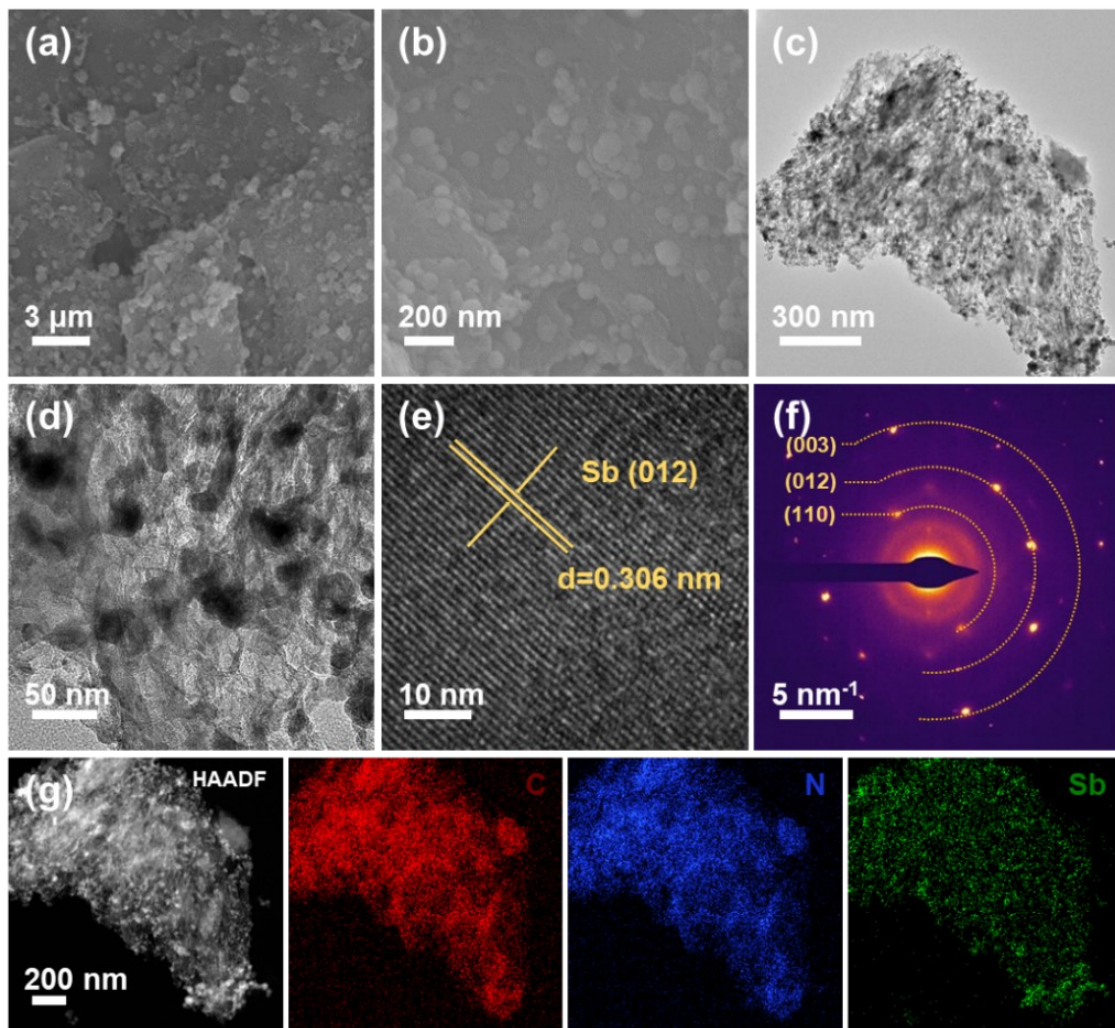


Figure S7. (a, b) SEM images and (c, d) TEM images of Sb NP@NC samples. (e) HRTEM and (f) the SAED patterns of Sb NP@NC. (g) STEM-HAADF images with corresponding EDS elemental mapping of Sb NP@NC.

Figure S8

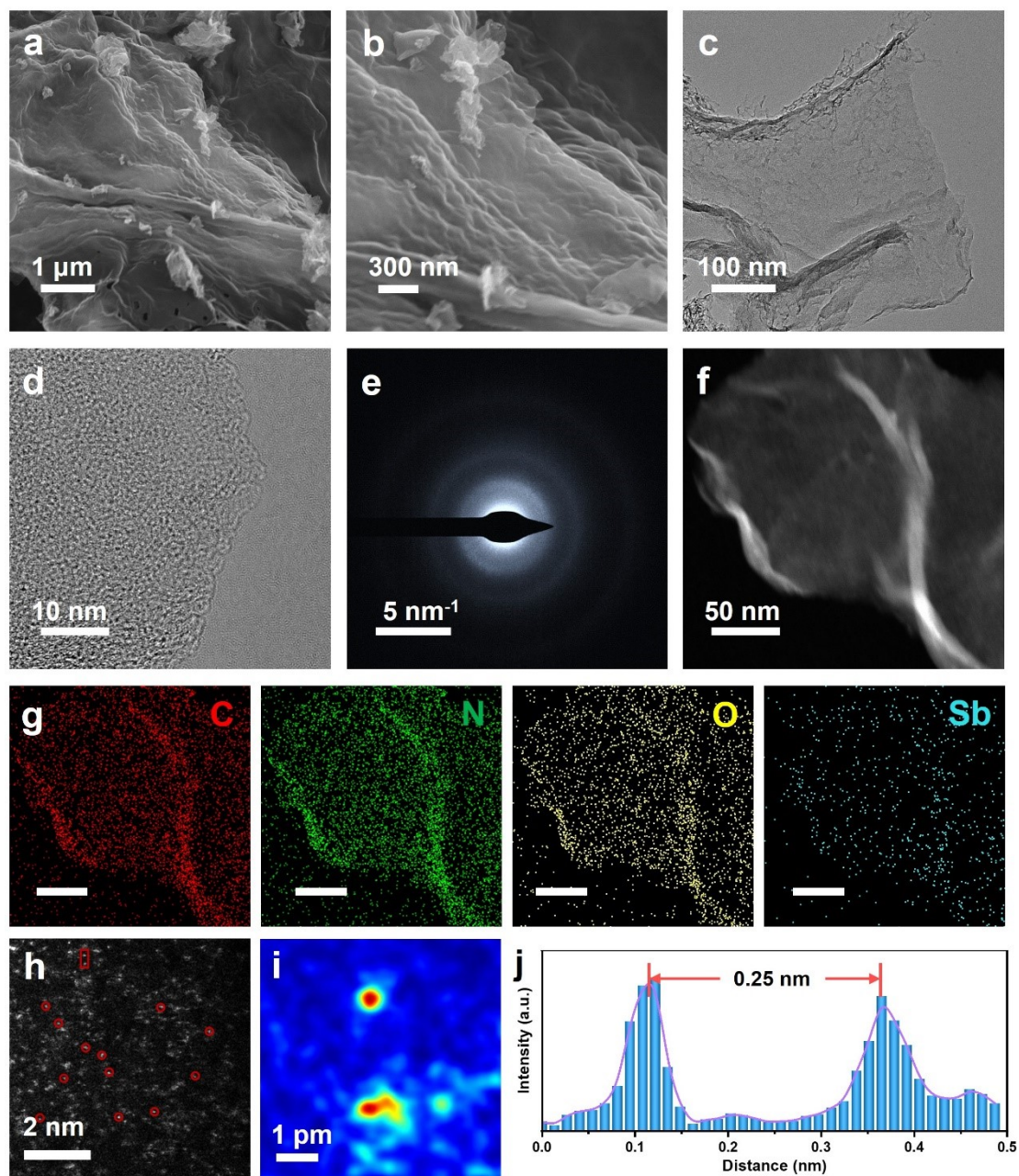


Figure S8. (a, b) SEM images and (c, d) TEM images of O-Sb-N SA@NC₁ samples. (e) The SAED patterns of O-Sb-N SA@NC₁. (f, g) HAADF-STEM images with corresponding EDS elemental mapping of O-Sb-N SA@NC₁. (h) Atomic resolution HAADF-STEM images of O-Sb-N SA@NC₁. (i) The gaussian fitting pattern of atomic distance in selected area in (h). (j) The intensity profiles of selected area in (h).

Figure S9

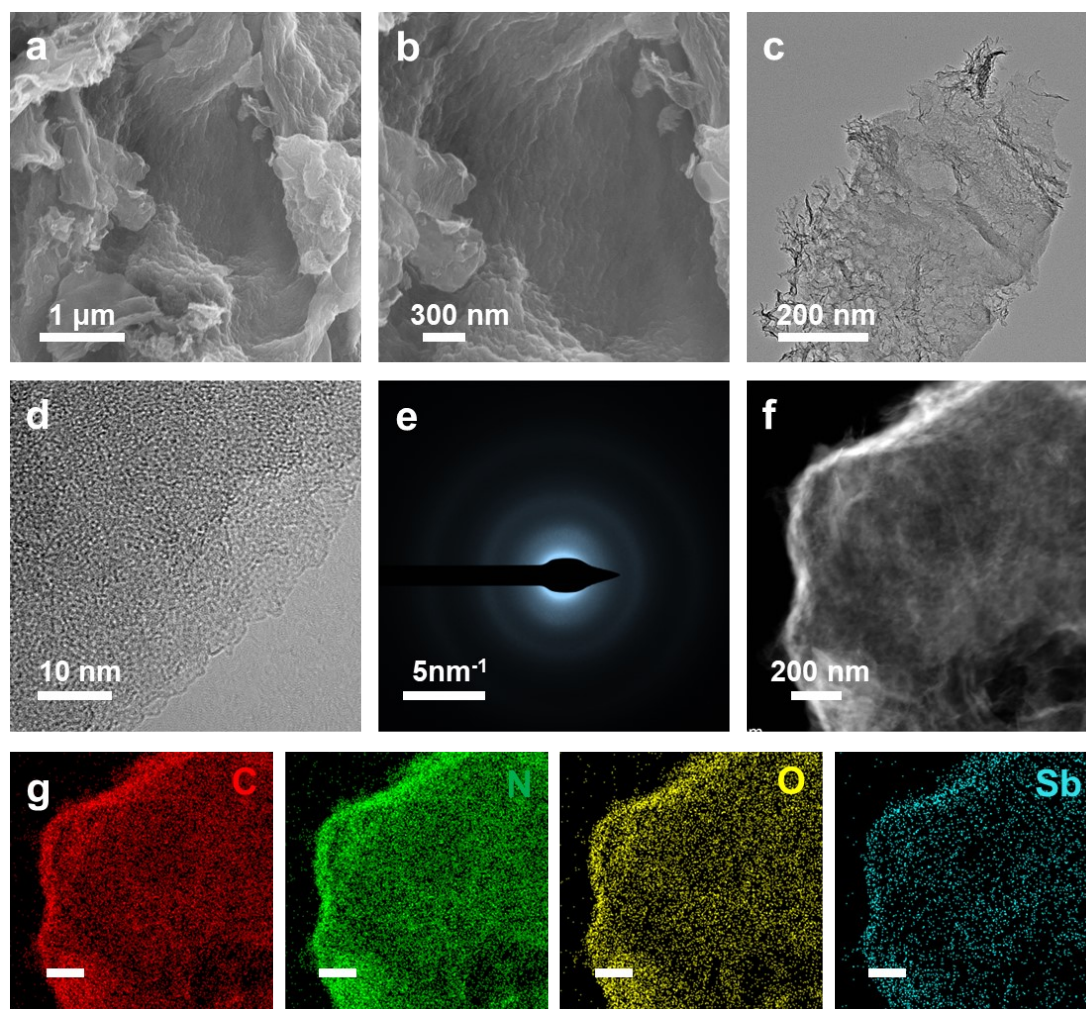


Figure S9. (a, b) SEM images and (c, d) TEM images of O-Sb-N SA@NC₃ samples. (e) The SAED patterns of O-Sb-N SA@NC₃. (f, g) HAADF-STEM images with corresponding EDS elemental mapping of O-Sb-N SA@NC₃.

Figure S10

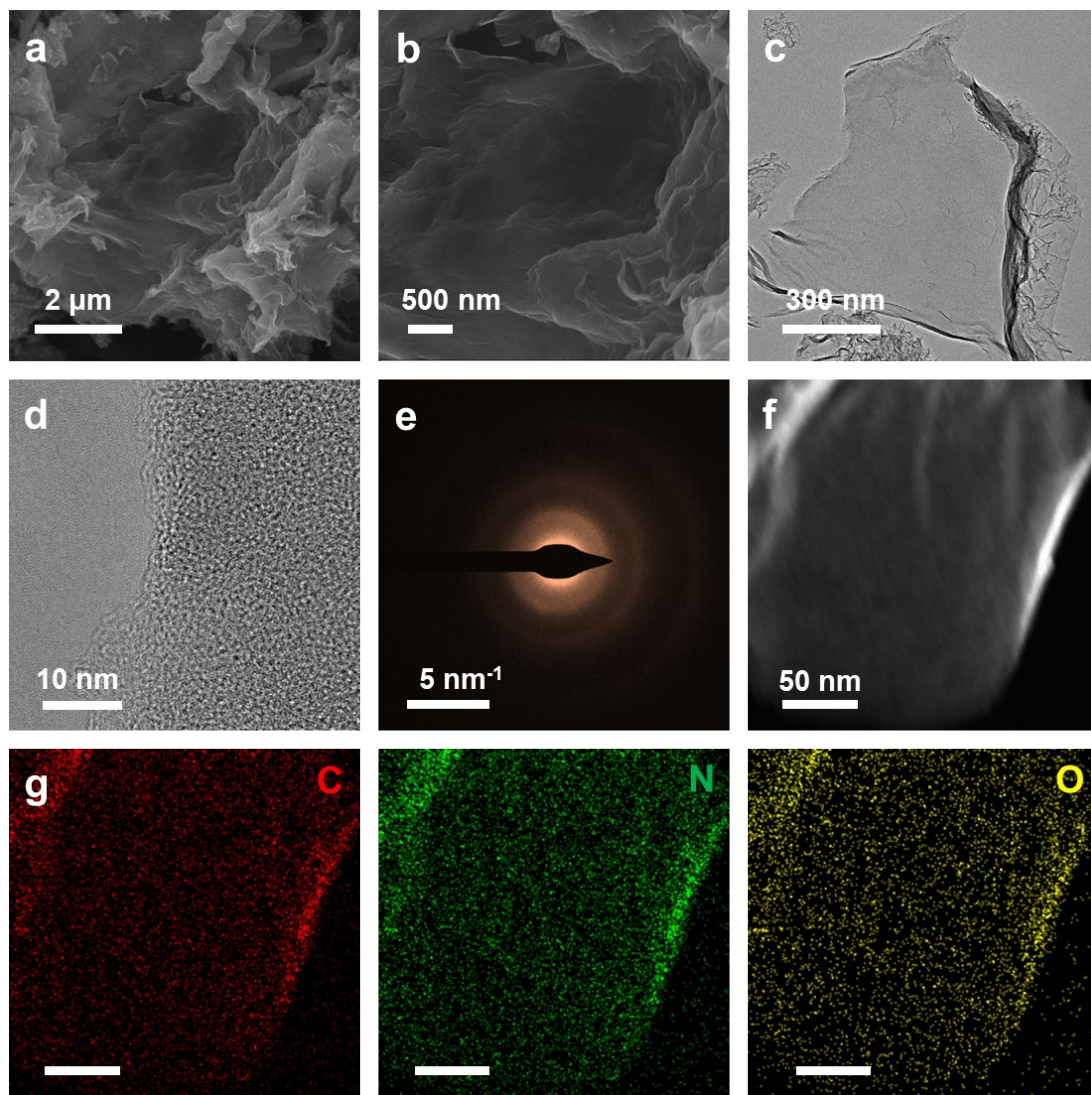


Figure S10. (a, b) SEM images and (c, d) TEM images of bare-NC samples. (e) The SAED patterns of bare-NC. (f, g) HAADF-STEM images with corresponding EDS elemental mapping of bare-NC.

Figure S11

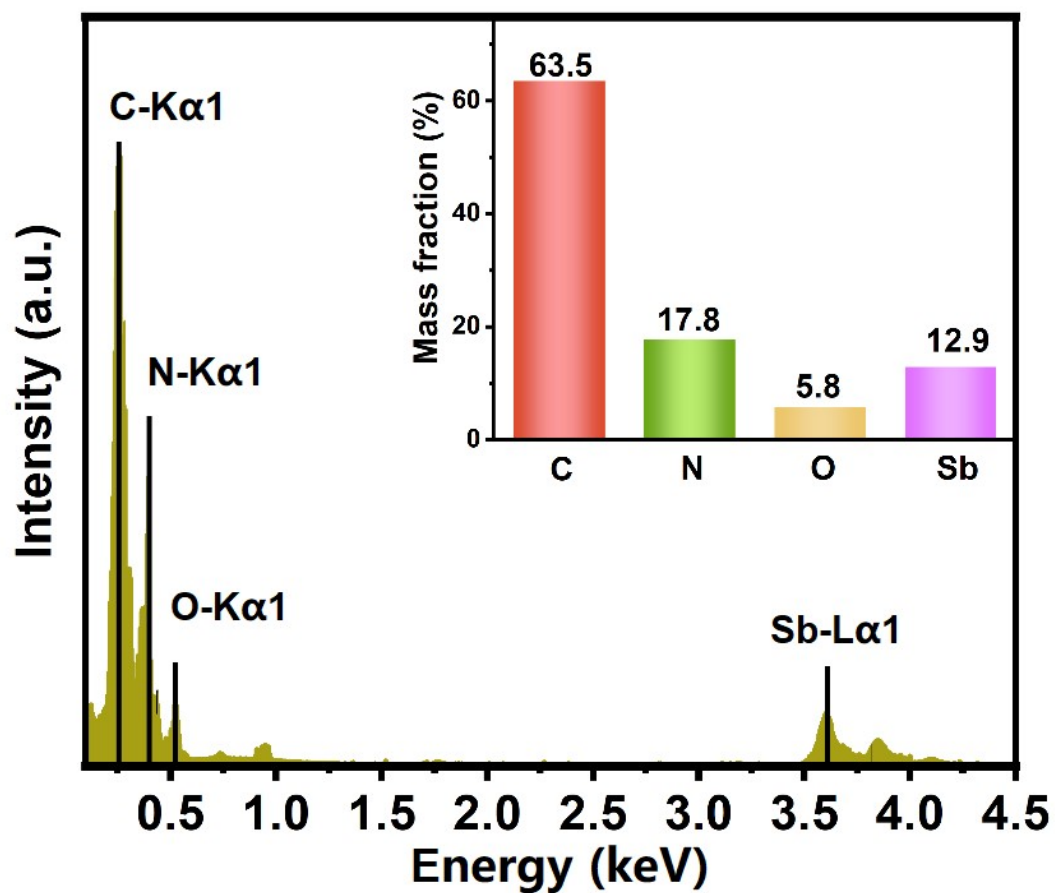


Figure S11. EDS spectrum and its inset showing the element contents of O-Sb-N SA@NC₂.

Figure S12

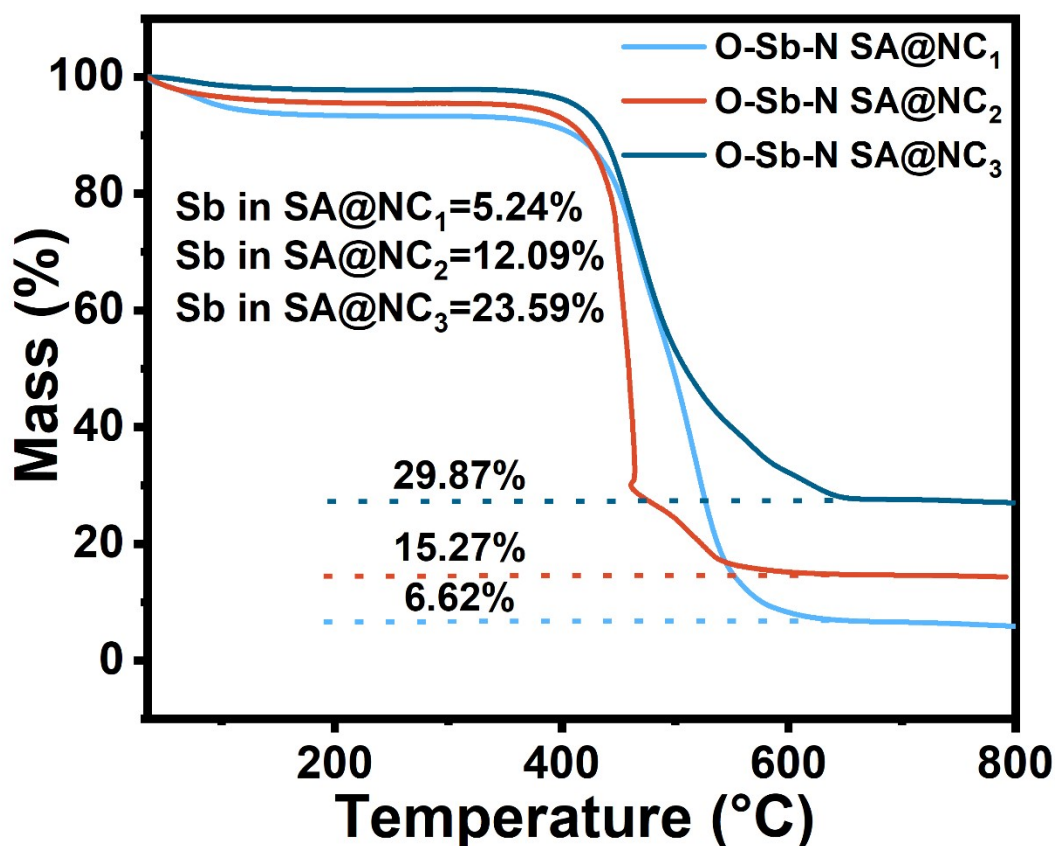
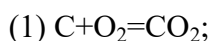


Figure S12. TGA curves of O-Sb-N SA@NC_s.

The TGA curves of O-Sb-N SA@NCs in Figure S12 reflect the weight loss of carbon combustion and the weight gain of Sb₂O₄ formation based on the following reactions:



The weight ratio of Sb in the nanocomposite was calculated to be 12.09% based on the following equation:

$$Sb(\text{wt.}\%) = \frac{\text{molecular weight of Sb}}{\text{molecular weight of Sb}_2\text{O}_4} \times \frac{\text{final weight of Sb}_2\text{O}_4}{\text{initial weight of Sb SA/NC}}$$

Equation S3

$$Sb(\text{wt.}\%) = \frac{121.76}{307.52} \times \frac{15.27}{100} \times 2 \times 100\% = 12.09\%$$

Figure S13

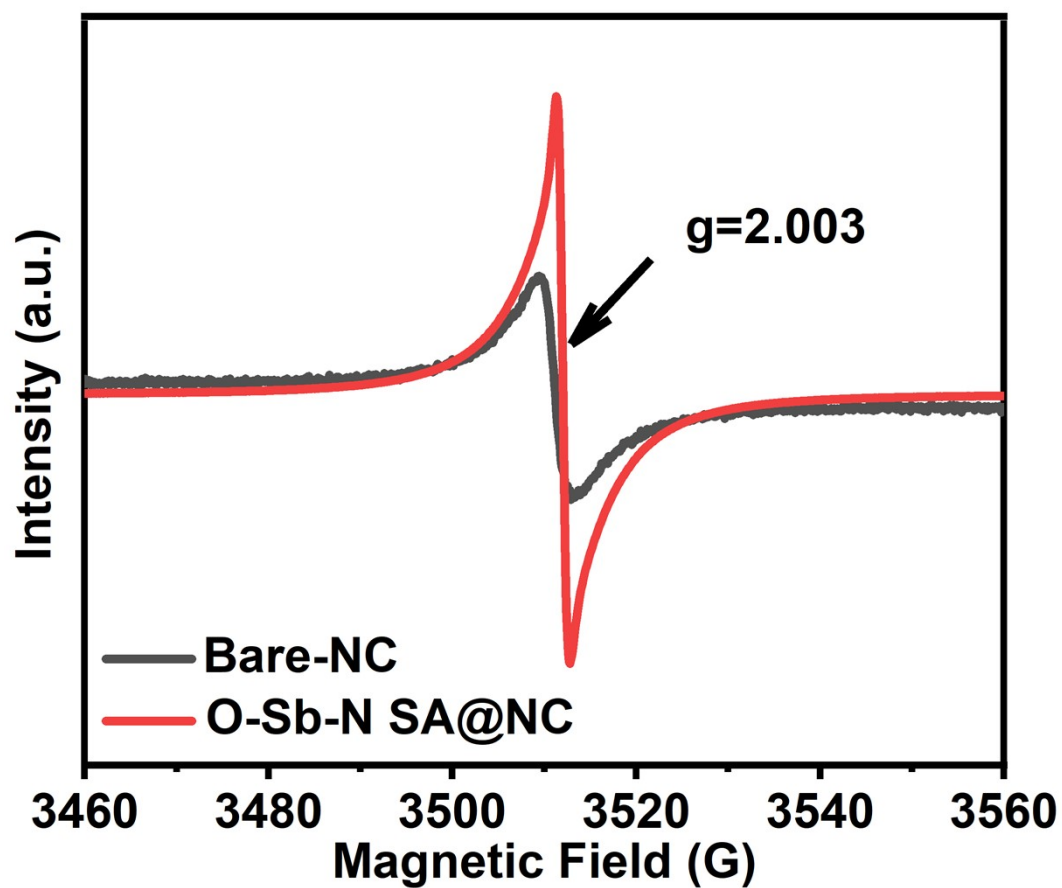


Figure S13. EPR results for O-Sb-N SA@NC₂ and bare-NC.

Figure S14

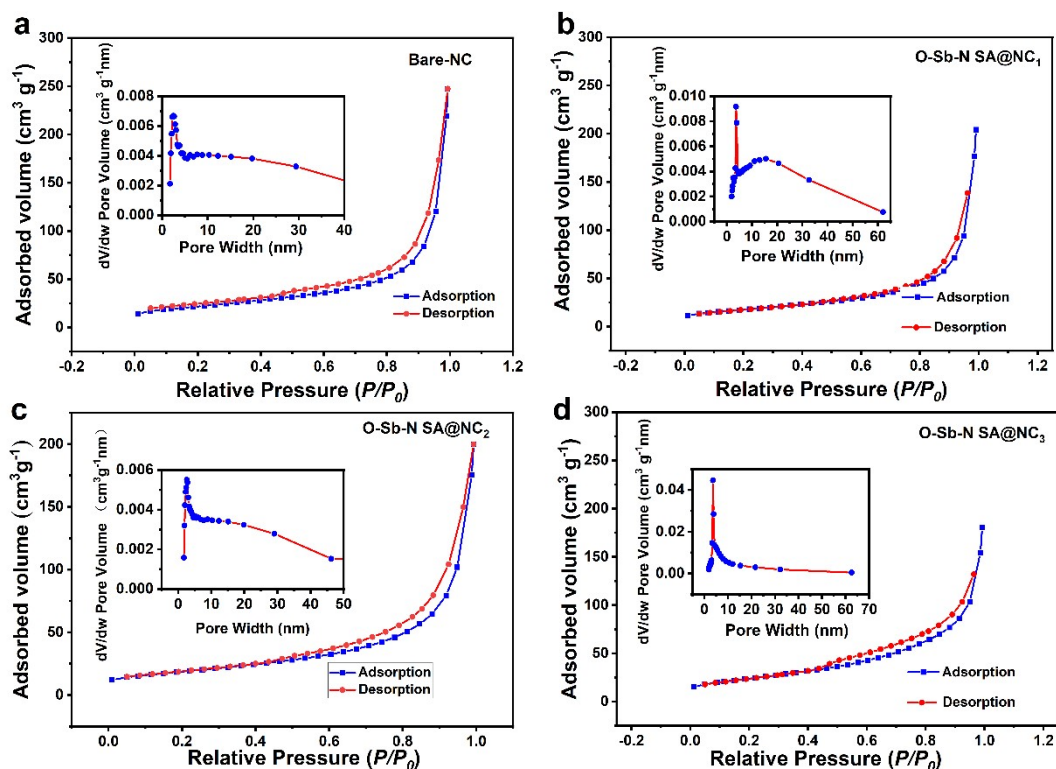


Figure S14. N_2 adsorption/desorption isotherms and the corresponding pore size distribution of (a) bare-NC, (b) O-Sb-N SA@NC₁, (c) O-Sb-N SA@NC₂ and (d) O-Sb-N SA@NC₃.

Figure S15

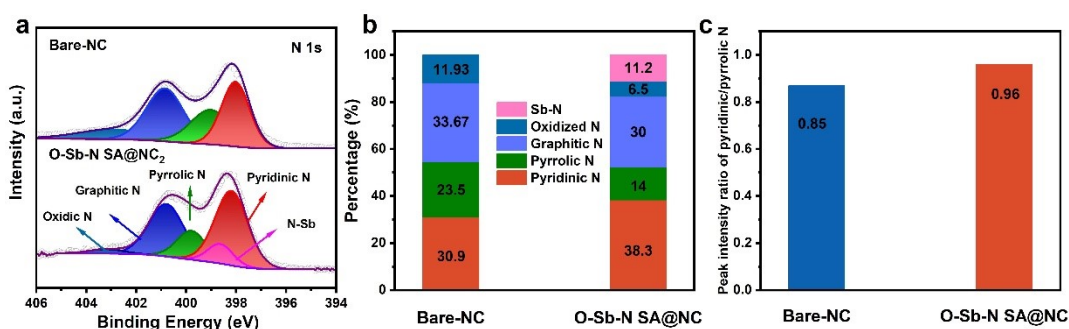


Figure S15. (a) High-resolution N 1s XPS spectra of O-Sb-N SA@NC₂ and Bare-NC. (b) Comparison of corresponding content of different types of N. (c) Comparison of corresponding peak intensity ratio of pyridinic N to pyrrolic N.

Figure S16

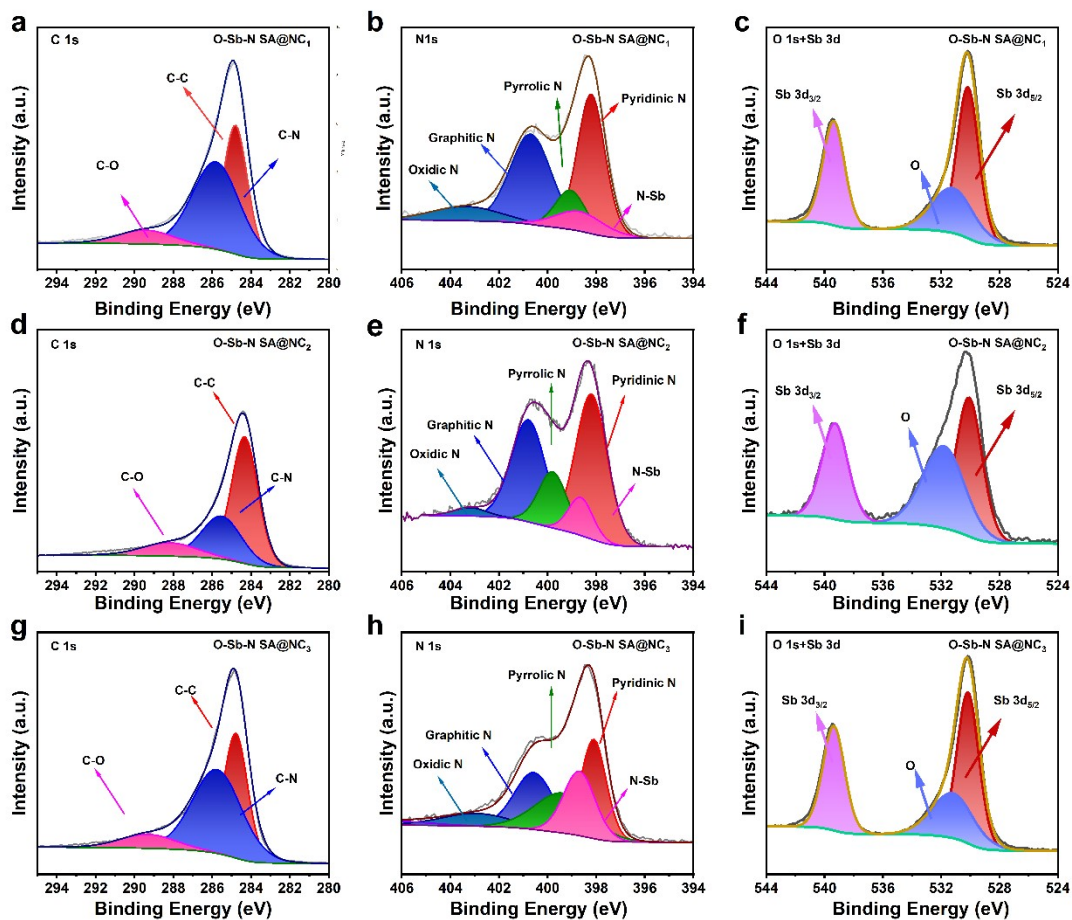


Figure S16. High-resolution XPS spectra of O-Sb-N SA@NC₁, O-Sb-N SA@NC₂ and O-Sb-N SA@NC₃.

Figure S17

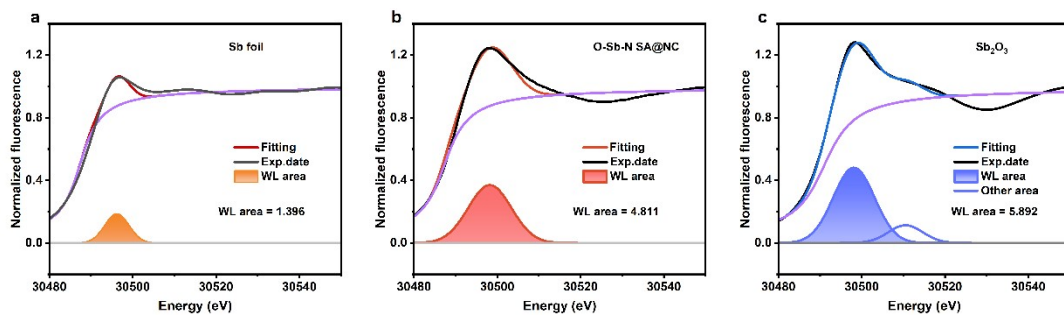


Figure S17. White line peak integral area of X-ray absorption near-edge of (a) Sb foil, (b) O-Sb-N SA@NC₂, and (c) Sb₂O₃.

Figure S18

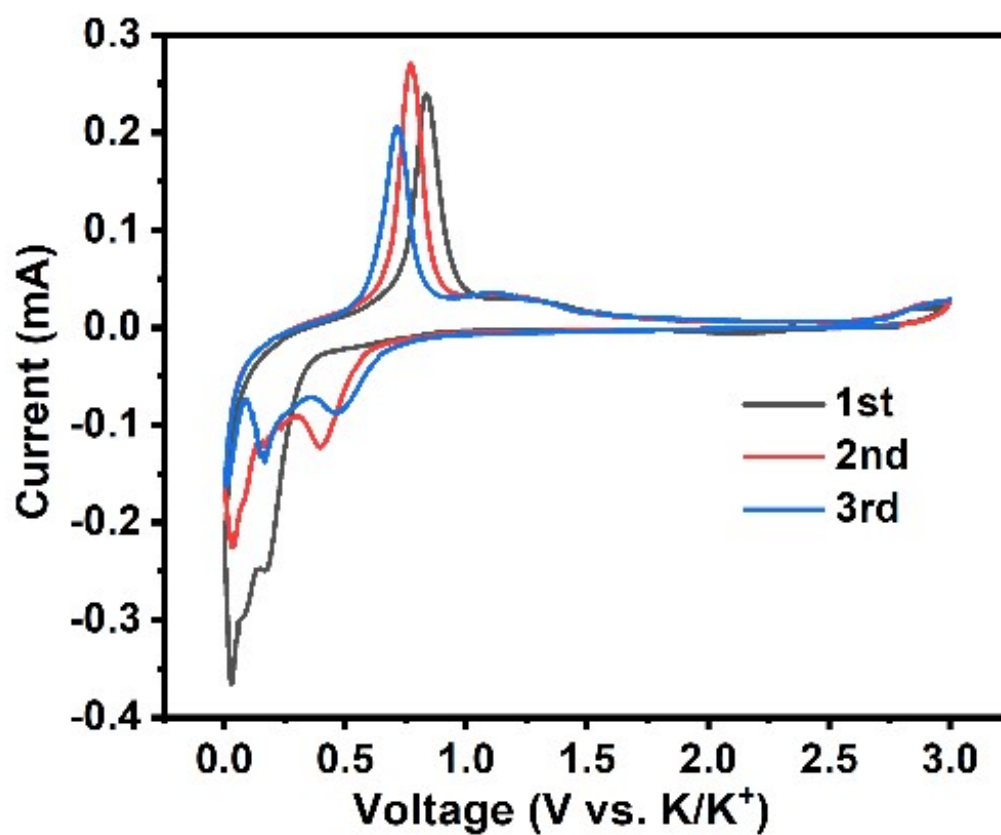


Figure S18. CV curves of the Sb NP@NC electrode at 0.1mV s^{-1} .

Figure S19

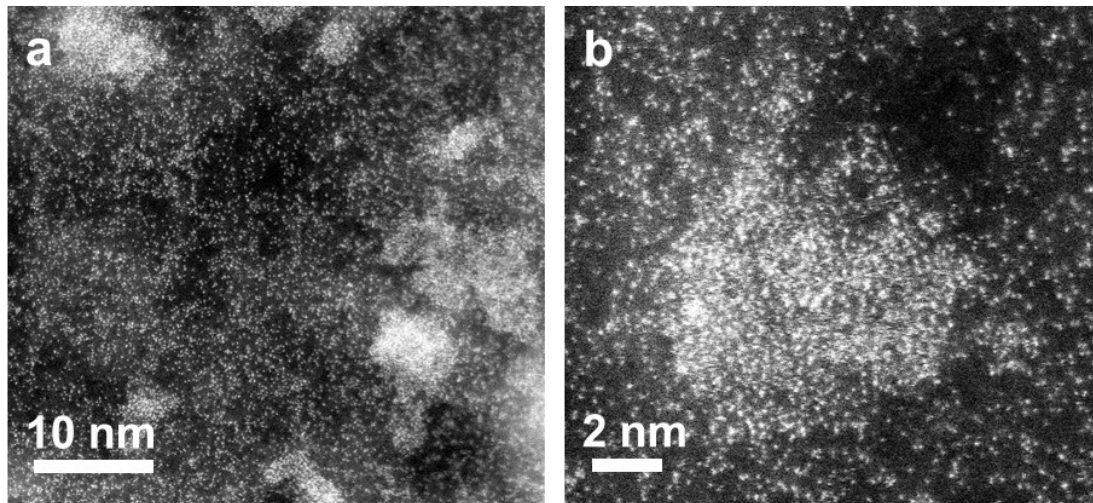


Figure S19. Atomic resolution HAADF-STEM images of O-Sb-N SA@NC₃.

Figure S20

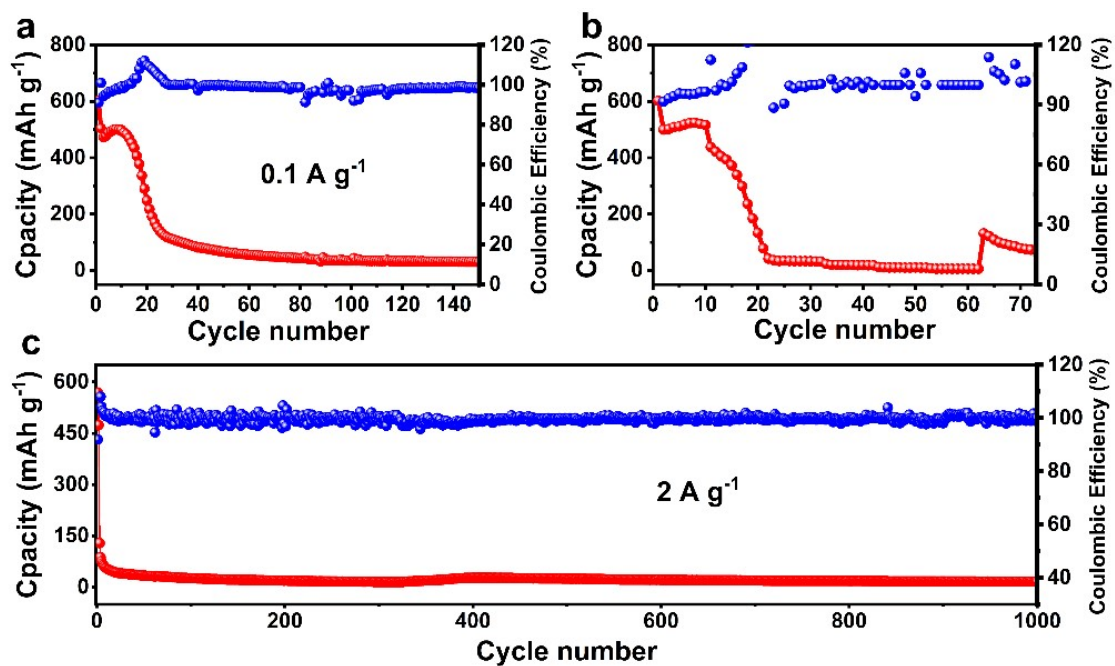


Figure S20. (a) Cycling performance at 100 mA g⁻¹, (b) rate capability at various current densities, and long-term cycling performance at 2 A g⁻¹ for the Sb NP@NC electrode.

Figure S21

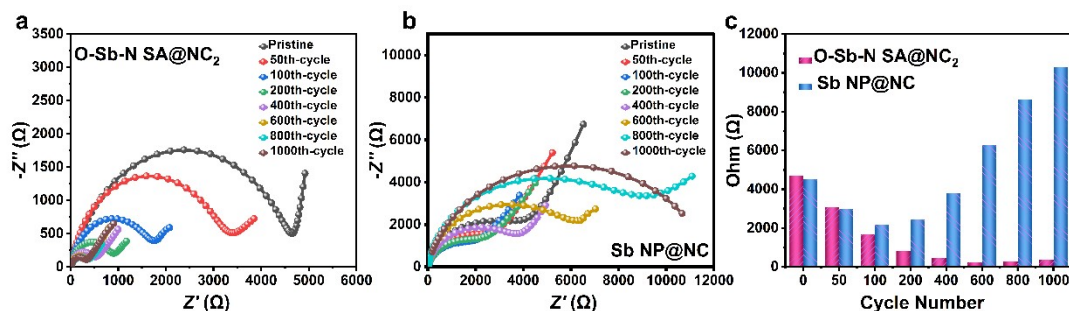


Figure S21. The Nyquist fitting plots of (a) O-Sb-N SA@NC₂ and (b) Sb NP@NC in different cycles. (c) Comparison of R_{ct} values after fitting.

The EIS measurement was detected from 1st to 1000th cycles at 2 A g⁻¹ to investigate the kinetic change during cycling for the O-Sb-N SA@NC₂ electrodes as shown in Figure S21. Nyquist plots are composed mainly of two semicircular in high frequency and low frequency, with slope lines in the low-frequency range. The diameter of the semicircles in high and middle frequency is attributed to solid electrode interface resistance (R_{SEI}) and the charge transfer resistance (R_{ct}), respectively. Moreover, the slope line means Warburg impedance related to the semi-infinite diffusion of K⁺ ions into the electrode-electrolyte interface.

Figure S22

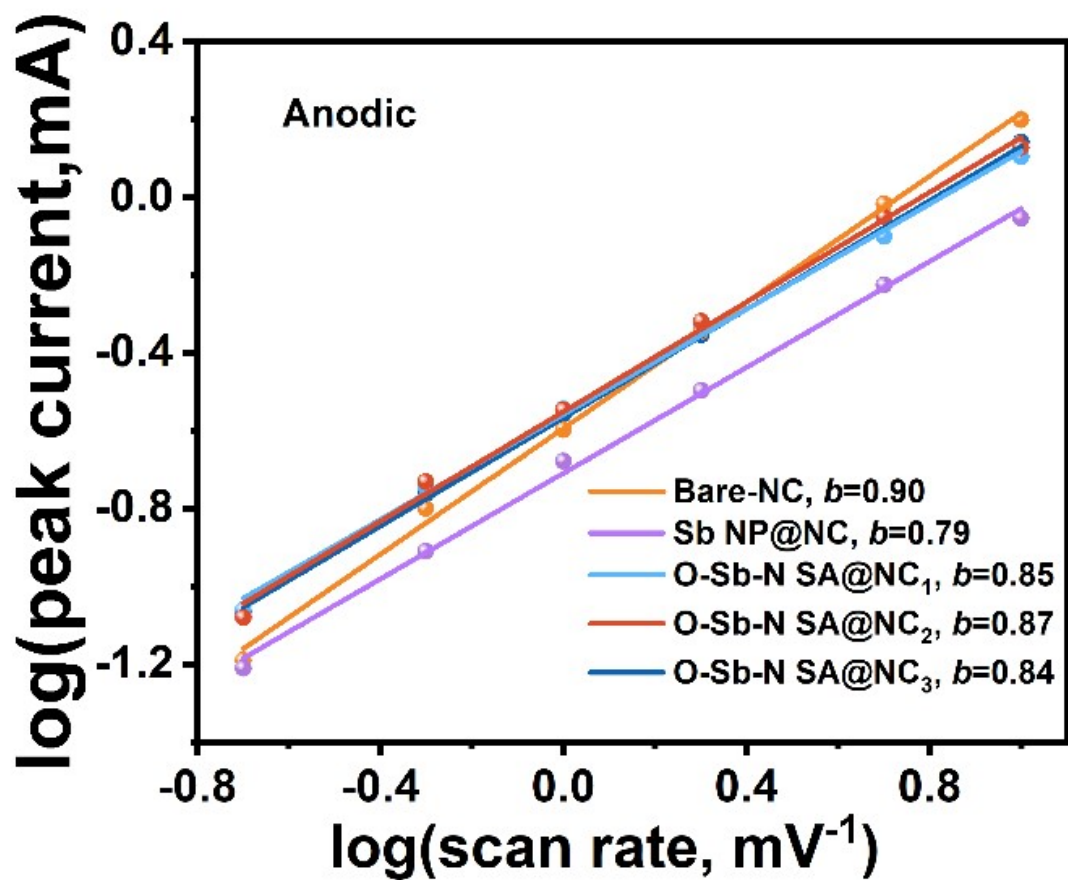


Figure S22. The plot of log (peak current) versus log (scan rate) of anodic peaks from CV scans and b-value determination lines.

Figure S23

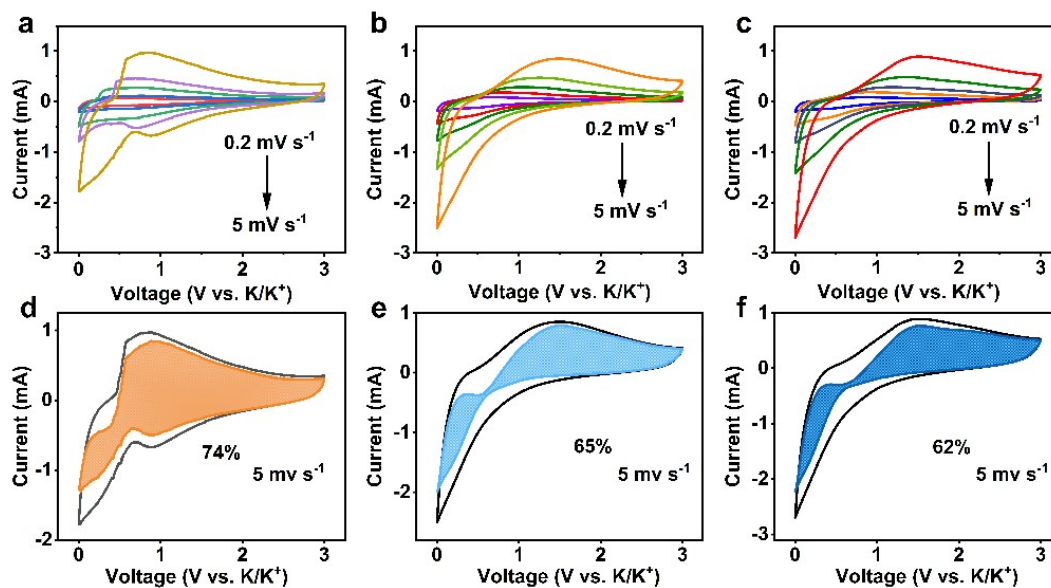


Figure S23. CV curves of the (a) bare-NC, O-Sb-N SA@NC₁ and (c) O-Sb-N SA@NC₃ electrodes at different scan rates. Contribution ratios of the capacitive process in (d) bare-NC, (e) O-Sb-N SA/NC₁, and (f) O-Sb-N SA@NC₃ at a scan rate of 5 mV s⁻¹.

Figure S24

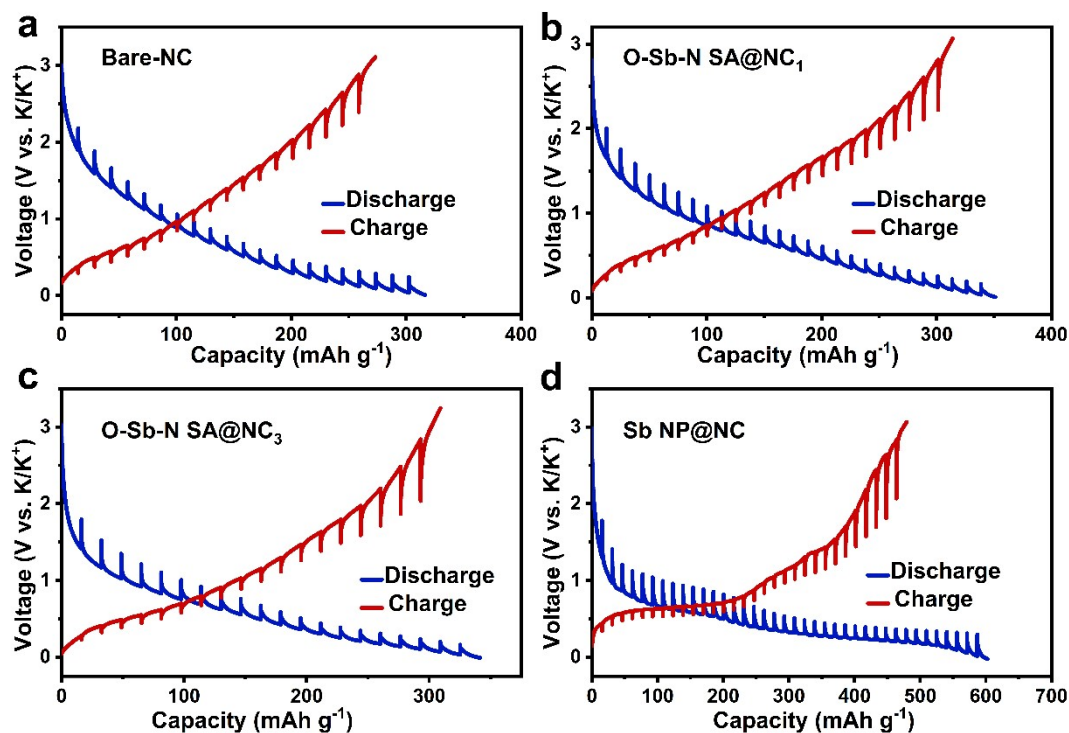


Figure S24. GITT potential profiles for (a) bare-NC, O-Sb-N SA@NC₁, (c) O-Sb-N SA@NC₃ and (d) Sb NP@NC electrodes

The diffusion coefficient (D) in bare-NC, Sb O-Sb-N SA@NCs, and Sb NP@NC are calculated from the galvanostatic intermittent titration technique (GITT) potential profiles using Fick's second law with the following equation:

$$D = \frac{4}{\pi\tau} \left(\frac{m_B V_M}{M_B S} \right)^2 \left(\frac{\Delta E_S}{\Delta E_t} \right)^2 \quad \text{Equation S4}$$

Where τ represents the duration of the current pulse; m_B is the electrode material mass loading; S represents the geometric area of the electrode; ΔE_S is the quasi-thermodynamic equilibrium potential difference between before and after the current pulse; ΔE_t is the potential difference during the current pulse; V_M is the molar volume of the active materials, and M_B is the molar mass of samples.

Figure S25

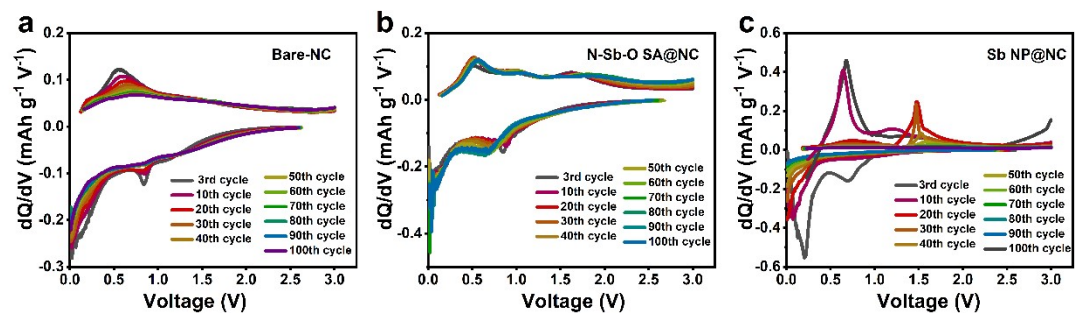


Figure S25. dQ/dV curves of Cycling performance of (a) bare-NC, (b) O-Sb-N SA@NC₂, and (c) Sb NP@NC electrodes at 0.1 A g^{-1} with different cycles.

Figure S26

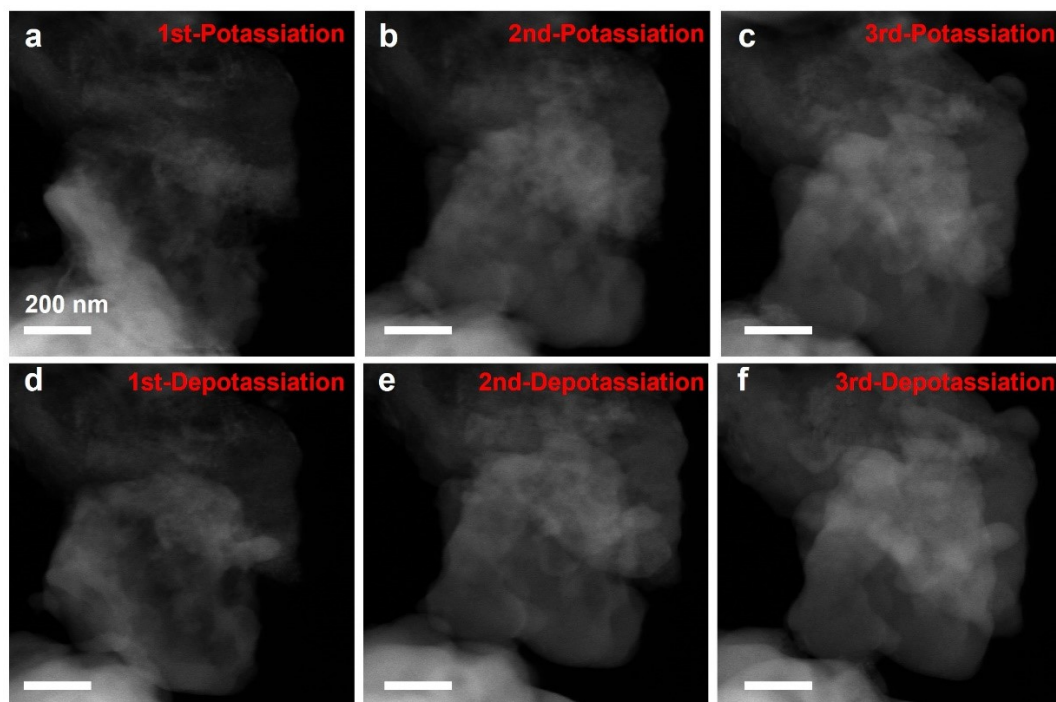


Figure S26. *In situ* dark field TEM images of O-Sb-N SA@NC₂ after (a) one potassiation and (d) one depotassiation, after (b) second potassiation and (d) second depotassiation, after (c) third potassiation and (f) third depotassiation.

Figure S27

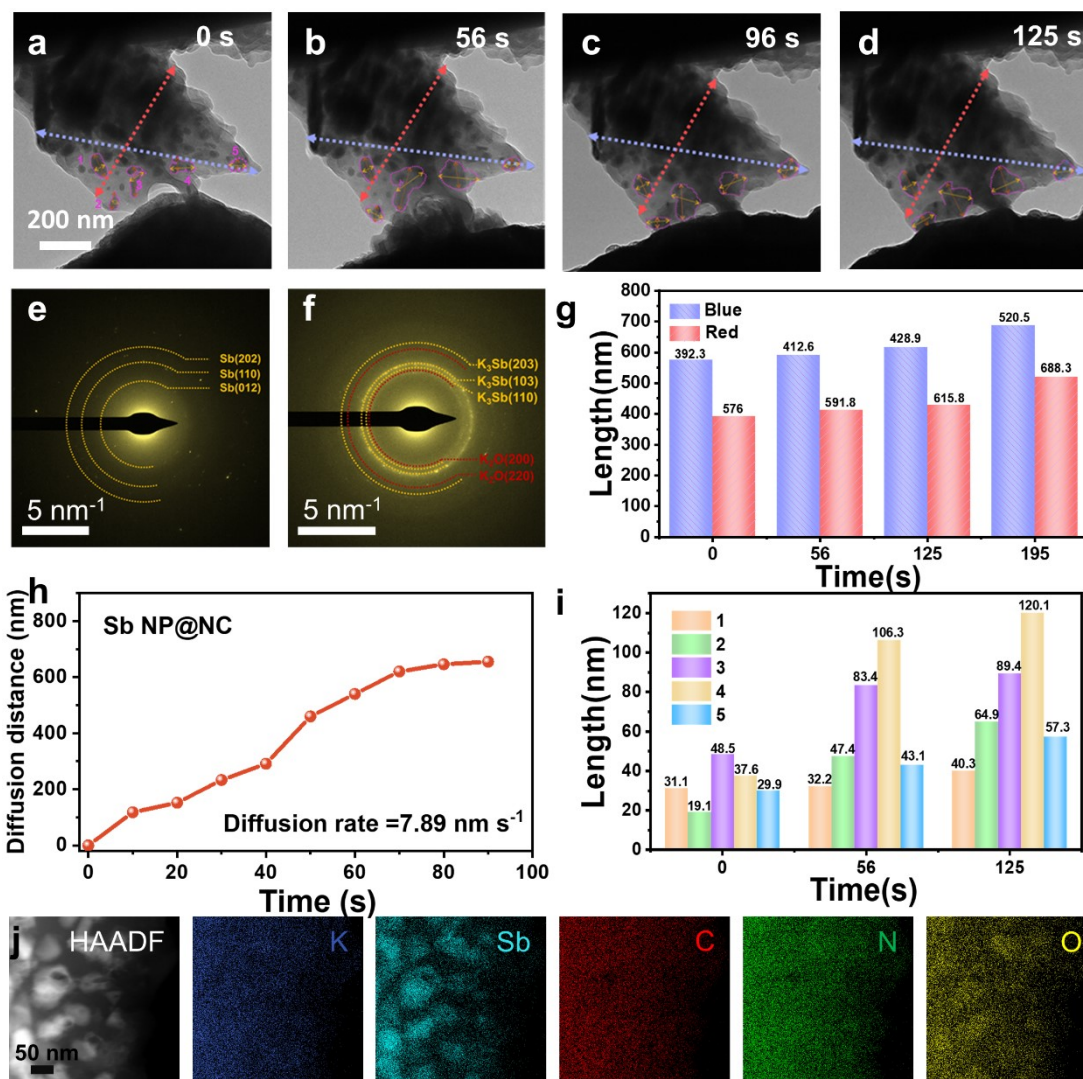


Figure S27. (a-d) *In situ* TEM images for Sb NP@NC electrode during potassiation. The corresponding SAED patterns of (e) pristine and (f) after full potassiation of Sb NP@NC. (g) The length evolution of Sb NP@NC. (h) The K⁺ diffusion speed of Sb NP@NC during potassiation (i) The histogram statistics of the increase of long axis length for corresponding Sb nanoparticles in Sb NP@NC. (j) HAADF-STEM images with their corresponding EDX element mapping.

Figure S28

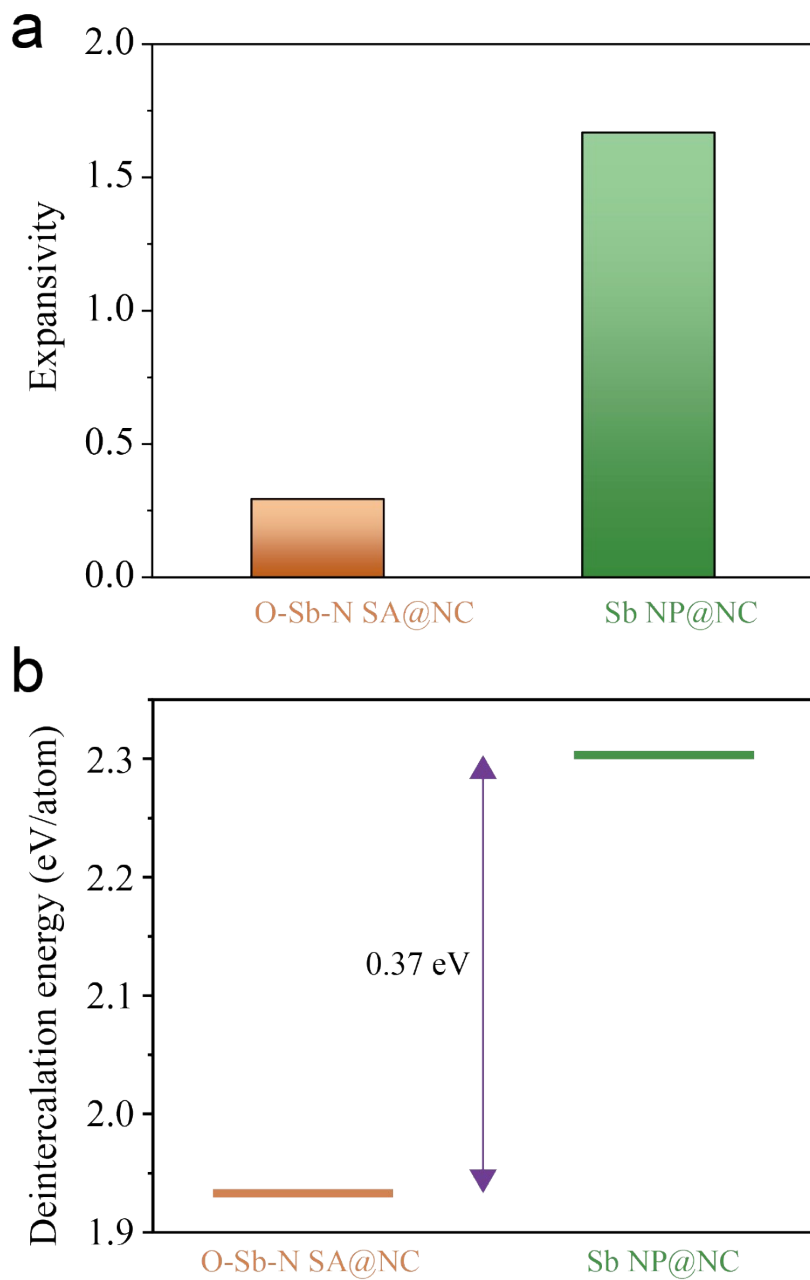


Figure S28. (a) Expansivity of O-Sb-N SA@NC and Sb NP@NC layers after the intercalation by the equal amount of K atoms. (b) Deintercalation Energy for one K atom extracted from O-Sb-N SA@NC and Sb NP@NC layers, respectively.

Figure S29

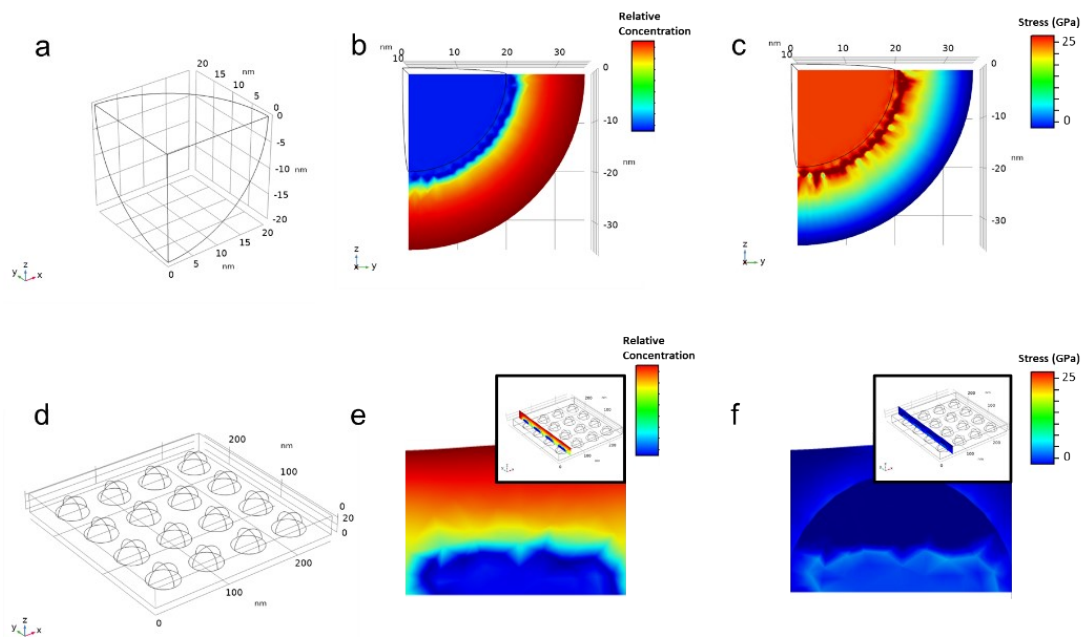


Figure S29. (a) The schematic showing the geometry of an Sb sphere in the FEA simulation and the corresponding (b) potassium concentration and (c) stress during the potassiation of the Sb sphere; (d) the geometry of the large Sb sphere embedded in a carbon sheet (Sb sphere/C) for the FEA simulation, and the corresponding (e) potassium concentration and (f) stress in the vicinity of an Sb sphere in the Sb sphere/C during the potassiation, the insets exhibit a cut plane of the Sb Sphere/C where the potassium concentration and stress were simulated and plotted;

Figure S30

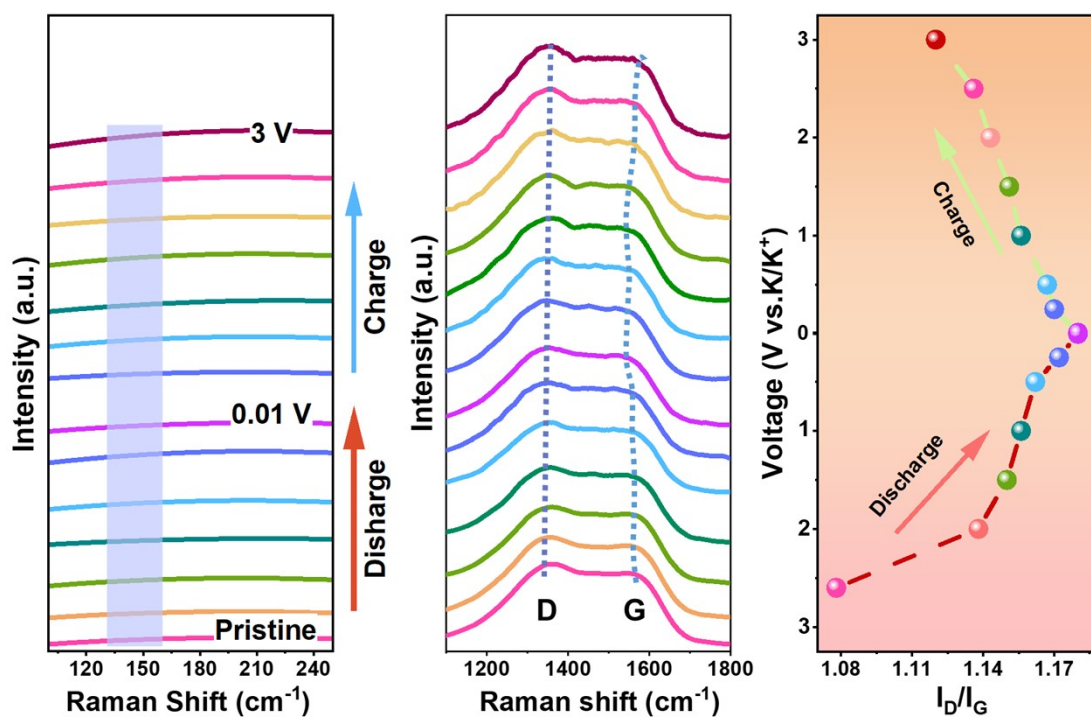


Figure S30. *In situ* Raman spectra of O-Sb-N SA@NC₂ in different voltage states and corresponding potential dependent I_D/I_G .

Figure S31

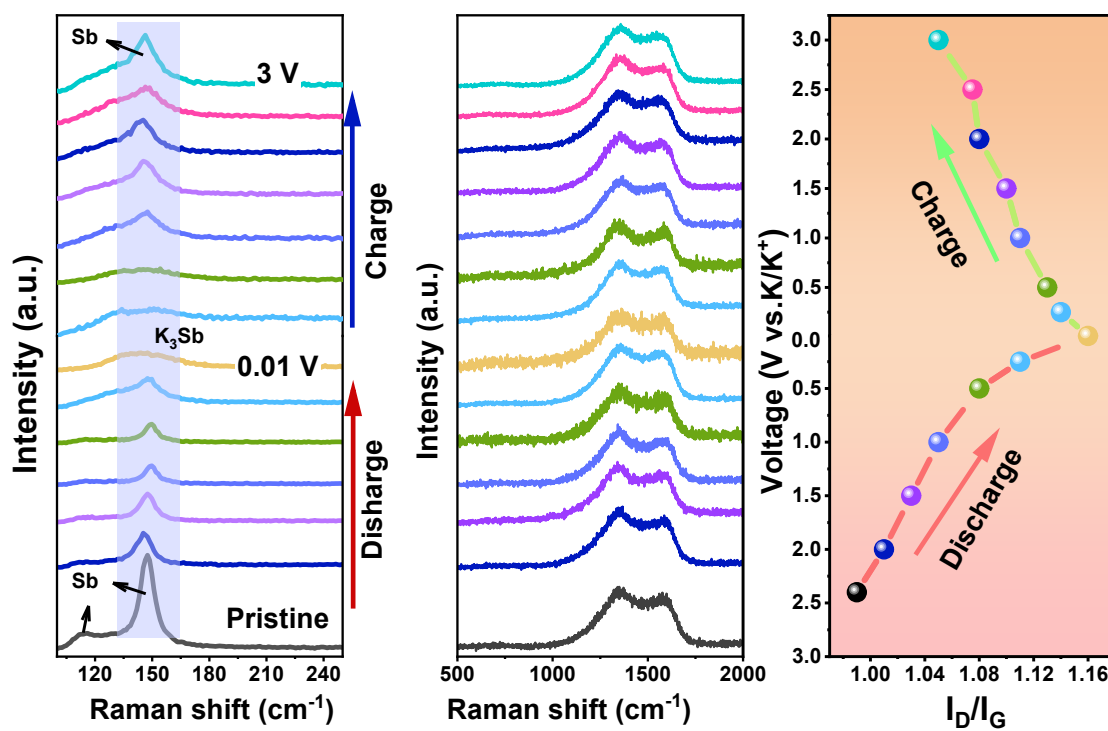


Figure S31. *Ex situ* Raman spectra of Sb NP@NC in different voltage states and its related potential dependent I_D/I_G curves.

Figure S32

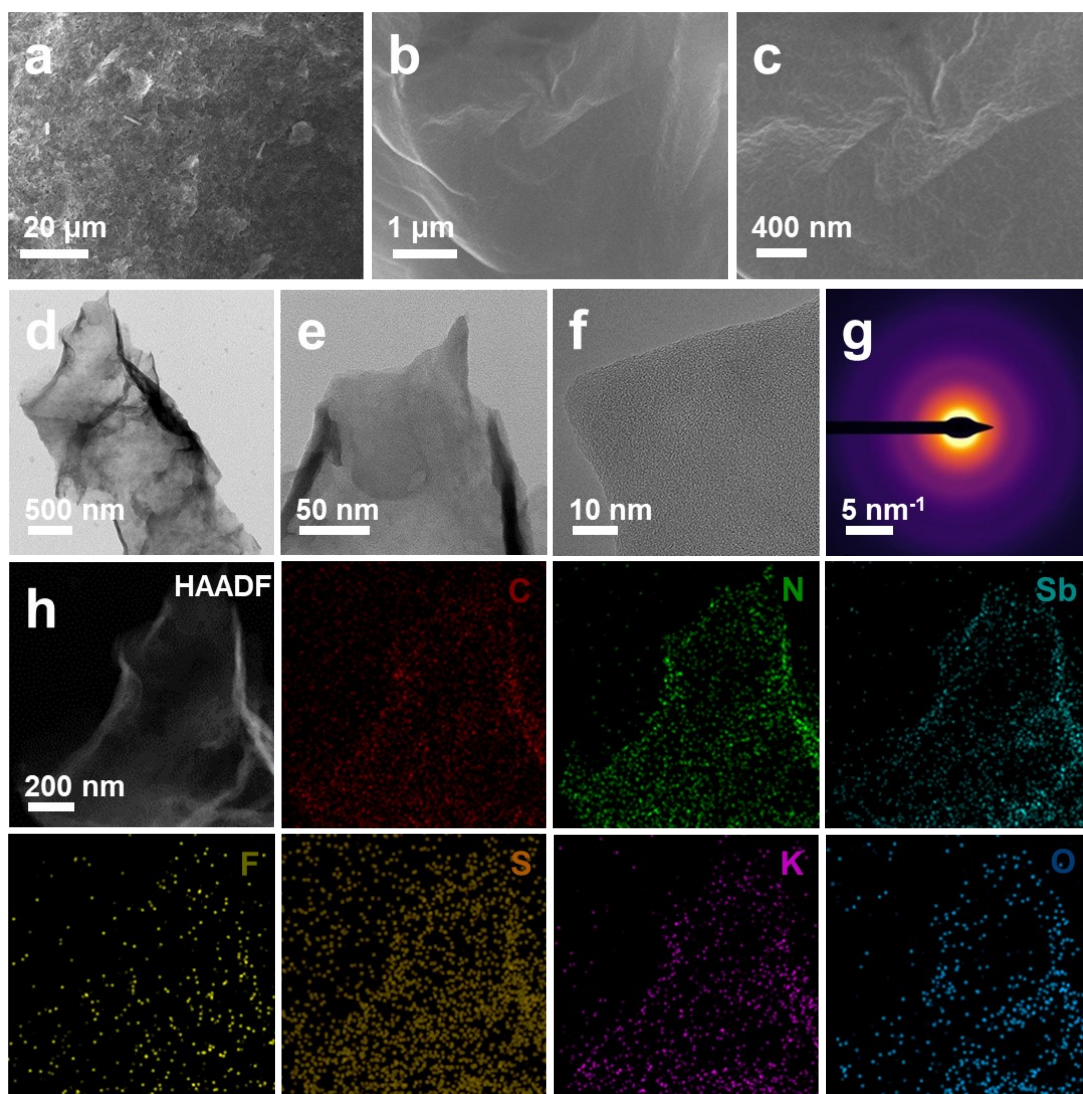


Figure S32. (a-c) SEM images, (d-f) TEM images and (g) SAED patterns, and (h) HAADF-STEM image and EDX elemental mapping images of O-Sb-N SA@NC₂ electrode at 2 A g⁻¹ over 1000 cycles.

Figure S33

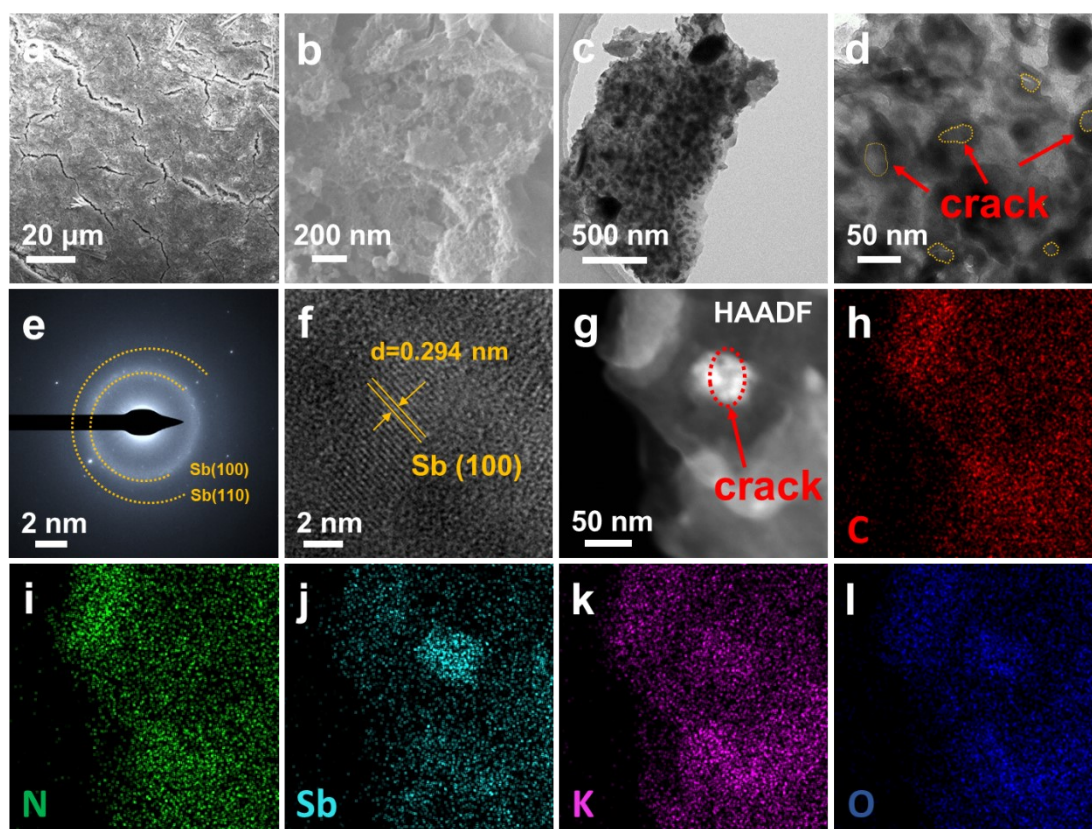


Figure S33. (a-b) SEM images, (c, d, f) TEM images, (e) SAED patterns, and (g-l) HAADF-STEM images and EDX elemental mapping images of Sb NP@NC electrode at 2 A g^{-1} over 1000 cycles.

Figure S34

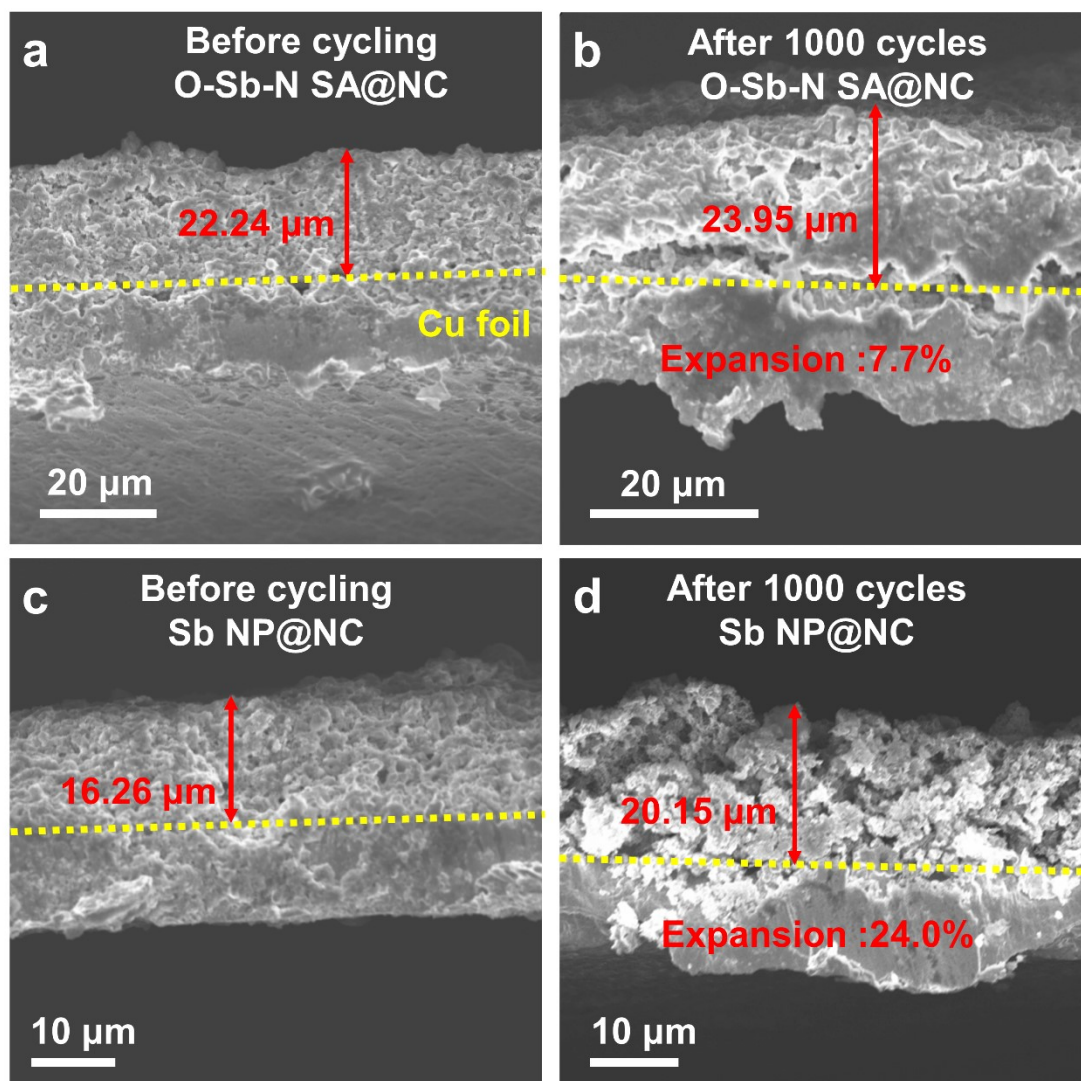


Figure S34. Electrode thickness before and after 1000 cycles at 2 Ag^{-1} : Cross section view SEM images before cycling (a) and after 1000 cycles (b) of O-Sb-N SA@NC₂. Cross section view SEM images before cycling (c) and after 1000 cycles (d) of Sb NP@NC.

Figure S35

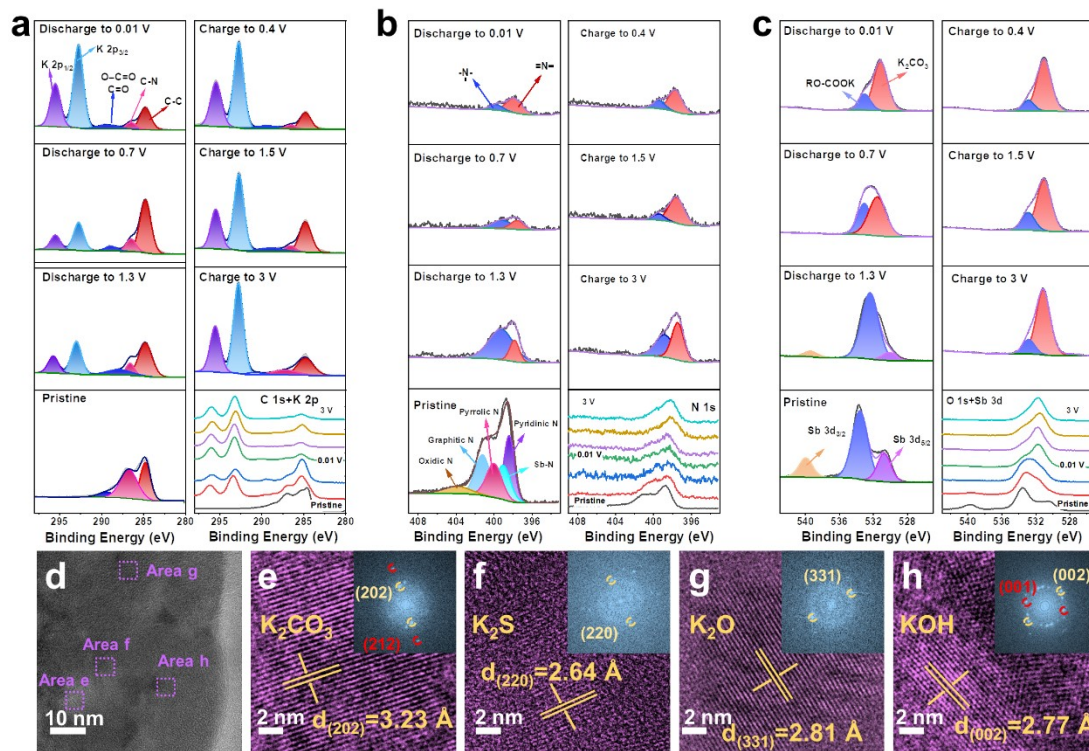


Figure S35. *Ex situ* XPS measurements of the cycled electrodes. (a) C 1s +K 2p. (b) N 1s and (c)O 1s + Sb 3d peaks of the electrodes;(d) HRTEM images of O-Sb-N SA@NC₂ and (e-h) its enlarged images marked in (d) after full potassiation observed by ultralow dosage cryo-TEM technique.

To clearly investigate the SEI formation on the surface of O-Sb-N SA@NC₂ electrodes, *ex situ* XPS and cryo-TEM were performed. As illustrated in figure S35a, for C 1s + K 2p spectrum, the peaks belonging to K 2p occur and remain stable during the cycling process, which originates from the K elements formatting SEI films⁹. As for Sb 3d and O 1s (Figure S35c), a new peak at about 531.5 eV appears during the potassiation process, corresponding to the formation of K₂CO₃. Note that the detection depth of XPS measurement is only several nanometers. Thus, the signal of Sb will be covered and disappear once an intact SEI is formed (Figure S35c). To precisely study the component of SEI, we directly froze the electrode after the full potassiation without any washing treatment and then transferred it to cryo-TEM. According to HRTEM analysis (Figure S35d-g), it is found that the SEI is mainly composed of K₂CO₃, K₂S, K₂O, and KOH, which matched well with the *ex situ* XPS results¹⁰.

Figure S36

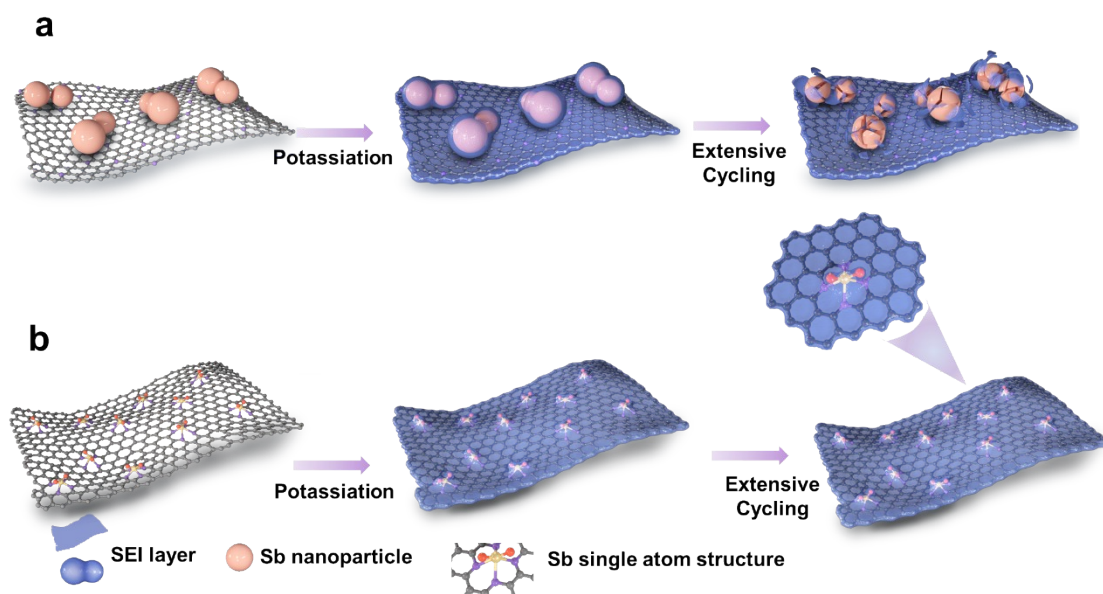


Figure S36. Schematic illustration of the morphology evolutions of (a) Sb NP@NC and (b) O-Sb-N SA@NC₂ electrodes during cycling.

Figure S37

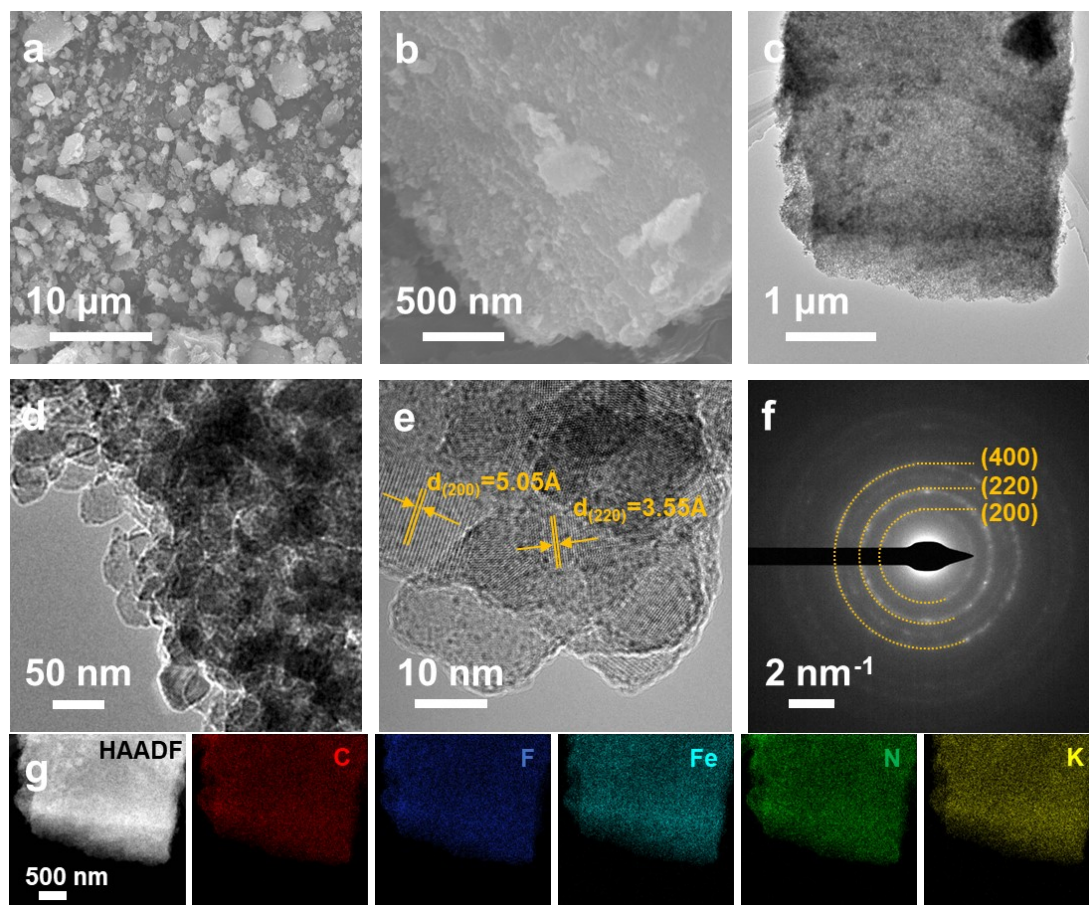


Figure S37. (a, b) SEM images, (c, d) TEM images, (e) HRTEM image and (f) the SAED patterns of KFeHCF. (g) HAADF-STEM image and element mapping images of KFeHCF.

Figure S38

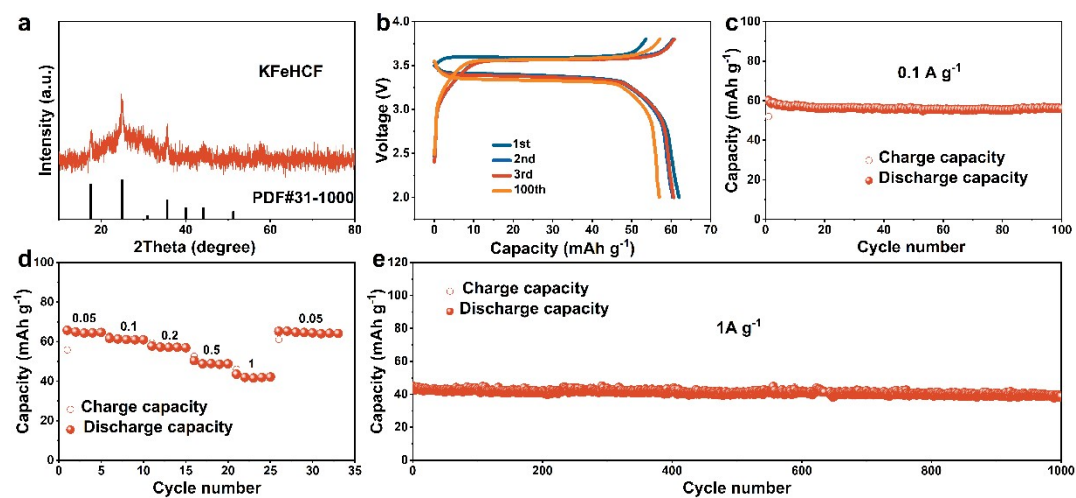


Figure S38. (a) XRD pattern of KFeHCF. The charge/discharge curves (b) and (c) cycling performance of KFeHCF cathode at 0.1 A g⁻¹. (d) Rate performance at various current densities and (e) long-term cycling performance of KFeHCF cathode at 1 A g⁻¹

Table S1. ICP-MS analysis of the atomic Sb contents in O-Sb-N SA@NCs.

Samples	Sb mass loading (%)
O-Sb-N SA@NC ₁	5.8
O-Sb-N SA@NC ₂	14.6
O-Sb-N SA@NC ₃	28.5

Table S2. Specific surface area and the corresponding pore size of bare-NC, O-Sb-N SA@NC₁, O-Sb-N SA@NC₂, O-Sb-N SA@NC₃.

Samples	specific surface area(m ² /g)	average pore diameter (nm)
Bare-NC	554.8184	9.0856
O-Sb-N SA@NC ₁	557.4147	9.5654
O-Sb-N SA@NC ₂	647.8137	9.3570
O-Sb-N SA@NC ₃	780.4587	7.4259

Table S3. Structural parameters extracted from the Sb K-edge EXAFS fitting

Catalysts	Scattering Path	CN	R (Å)	R-factor	ΔE_0 (eV)	σ^2 (10^{-3}\AA^2)
Sb-sample	Sb-N(O)	5.7	1.98	0.004	3.59	9

CN is the coordination number; R is the interatomic distance (the bond length between central atoms and surrounding coordination atoms); σ^2 is Debye-Waller factor (a measure of thermal and static disorder in absorber-scatterer distances); ΔE_0 is edge-energy shift (the difference between the zero kinetic energy value of the sample and that of the theoretical model). R factor is used to value the goodness of the fitting.

Table S4. The comparison of electrochemical performance of O-Sb-N SA@NC₂ with previously reported Sb -based and carbon-based composite anodes for PIBs.

Electrode materials	ICE (%)	Rate performance	Cycling performance	Ref.
Ultrahigh edge-N-doping C	61	518 mA h g ⁻¹ at 0.05 A g ⁻¹	291 mAh g ⁻¹ after 500 cycles at 1 A g ⁻¹	11
		436 mA h g ⁻¹ at 0.1 A g ⁻¹		
		378 mA h g ⁻¹ at 0.2 A g ⁻¹		
		313 mA h g ⁻¹ at 0.5 A g ⁻¹		
		265 mA h g ⁻¹ at 1 A g ⁻¹		
		212 mA h g ⁻¹ at 2 A g ⁻¹		
Defect-rich C	90.4	119 mA h g ⁻¹ at 5 A g ⁻¹	180.2 mAh g ⁻¹ after 5000 cycles at 1 A g ⁻¹ .	12
		425 mA h g ⁻¹ at 0.05 A g ⁻¹		
		362 mA h g ⁻¹ at 0.1 A g ⁻¹		
		314 mA h g ⁻¹ at 0.2 A g ⁻¹		
		267 mA h g ⁻¹ at 0.5 A g ⁻¹		
		240 mA h g ⁻¹ at 1 A g ⁻¹		
N, O-doped porous C spheres	45.0	215 mA h g ⁻¹ at 2 A g ⁻¹	107 mAh g ⁻¹ after 4000 cycles at 5 A g ⁻¹ .	13
		413.5 mA h g ⁻¹ at 0.1 A g ⁻¹		
		322.3 mA h g ⁻¹ at 0.2 A g ⁻¹		
		246.6 mA h g ⁻¹ at 0.5 A g ⁻¹		
		201.7 mA h g ⁻¹ at 1 A g ⁻¹		
		157.23 mA h g ⁻¹ at 2 A g ⁻¹		
N/O dual-doped hard C	50.7	105.5 mA h g ⁻¹ at 5 Ag ⁻¹	189.5 mAh g ⁻¹ at 1 A g ⁻¹ after 5000 cycles.	14
		439.1 mA h g ⁻¹ at 0.1 A g ⁻¹		
		336.5 mA h g ⁻¹ at 0.2 A g ⁻¹		
		286.7 mA h g ⁻¹ at 0.5 A g ⁻¹		
		254.4 mA h g ⁻¹ at 1 A g ⁻¹		
		223.4 mA h g ⁻¹ at 2 A g ⁻¹		
S/N dual-doped rich C	45.0	178.9 mA h g ⁻¹ at 5 Ag ⁻¹	141 mAh g ⁻¹ after 3000 cycles at 2 A g ⁻¹ .	15
		437 mA h g ⁻¹ at 0.1 A g ⁻¹		
		369 mA h g ⁻¹ at 0.2 A g ⁻¹		
		286 mA h g ⁻¹ at 0.5 A g ⁻¹		
		234 mA h g ⁻¹ at 1 A g ⁻¹		
		175 mA h g ⁻¹ at 2 A g ⁻¹		
3D Sb-NP@C	46.2	114 mA h g ⁻¹ at 5 A g ⁻¹	94 mA h g ⁻¹ after 200 cycles at 0.5 A g ⁻¹ .	16
		72 mA h g ⁻¹ at 10 A g ⁻¹		
		250 mA h g ⁻¹ at 0.1 A g ⁻¹		

			210 mA h g ⁻¹ at 0.2 A g ⁻¹ 170 mA h g ⁻¹ at 0.5 A g ⁻¹ 110 mA h g ⁻¹ at 1 A g ⁻¹		
Hierarchical porous CNF	78.9		327 mA h g ⁻¹ at 0.1 A g ⁻¹ 301 mA h g ⁻¹ at 0.2 A g ⁻¹ 288 mA h g ⁻¹ at 0.5 A g ⁻¹ 268 mA h g ⁻¹ at 1 A g ⁻¹ 246 mA h g ⁻¹ at 2 A g ⁻¹ 220 mA h g ⁻¹ at 5 A g ⁻¹ 194 mA h g ⁻¹ at 10 A g ⁻¹	305 mAh g ⁻¹ at 0.2 A g ⁻¹ after 300 cycles; 68 mAh g ⁻¹ at 2 A g ⁻¹ after 4000 cycles.	17
Micron-sized Sb	71.0		539 mA h g ⁻¹ at 0.05 A g ⁻¹ 400 mA h g ⁻¹ at 0.1A g ⁻¹ 242 mA h g ⁻¹ at 0.2 A g ⁻¹ 146 mA h g ⁻¹ at 0.3 A g ⁻¹ 81mA h g ⁻¹ at 0.4 A g ⁻¹ 30 mA h g ⁻¹ at 0.5 A g ⁻¹	318 mAh g ⁻¹ after 50 cycles at 0.5 A g ⁻¹ .	18
3D macroporous Sb@C	76.2		516 mA h g ⁻¹ at 0.05 A g ⁻¹ 447 mA h g ⁻¹ at 0.2A g ⁻¹ 388 mA h g ⁻¹ at 0.4 A g ⁻¹ 347 mA h g ⁻¹ at 0.8 A g ⁻¹ 286mA h g ⁻¹ at 1 A g ⁻¹	445 mA h g ⁻¹ after 150 cycles at 0.05 A g ⁻¹ ; 342 mAh g ⁻¹ after 260 cycles at 0.5 A g ⁻¹ .	19
N/O dual-doped C network	47		382 mA h g ⁻¹ at 0.05 A g ⁻¹ 319 mA h g ⁻¹ at 0.1A g ⁻¹ 268 mA h g ⁻¹ at 0.2 A g ⁻¹ 236 mA h g ⁻¹ at 0.5 A g ⁻¹ 205mA h g ⁻¹ at 1 A g ⁻¹ 181mA h g ⁻¹ at 2 A g ⁻¹	260 mAh g ⁻¹ after 100 cycle at 0.1 A g ⁻¹ . 160 mAh g ⁻¹ after 4000 cycle of 1.0 A g ⁻¹ .	20
Sn-Sb compounds with novel structure	/		479 mA h g ⁻¹ at 0.1 A g ⁻¹ 415 mA h g ⁻¹ at 0.2A g ⁻¹ 320 mA h g ⁻¹ at 0.5 A g ⁻¹ 250 mA h g ⁻¹ at 1 A g ⁻¹ 173mA h g ⁻¹ at 2 A g ⁻¹ 118mA h g ⁻¹ at 5 A g ⁻¹	296 mA h g ⁻¹ after 150 cycles at 0.5 A g ⁻¹ .	21
Active sites enriched hard C	49.0		468 mA h g ⁻¹ at 0.05 A g ⁻¹ 407 mA h g ⁻¹ at 0.1A g ⁻¹ 367 mA h g ⁻¹ at 0.2 A g ⁻¹ 328 mA h g ⁻¹ at 0.4 A g ⁻¹ 286mA h g ⁻¹ at 0.8 A g ⁻¹	379 mAh g ⁻¹ after 120 cycles at 0.2 A g ⁻¹ ; 277 mAh g ⁻¹ after 1600 cycles at 1 A g ⁻¹ .	22

			235mA h g ⁻¹ at 1.6 A g ⁻¹		
3D CFM-SNG	/		306 mA h g ⁻¹ at 0.05 A g ⁻¹ 279.2 mA h g ⁻¹ at 0.1A g ⁻¹ 269.1 mA h g ⁻¹ at 0.2 A g ⁻¹ 245 mA h g ⁻¹ at 0.5 A g ⁻¹ 222.7 mA h g ⁻¹ at 1A g ⁻¹	348.2 mA h g ⁻¹ at 0.1A g ⁻¹ after 160 cycles; 188.8 mAh g ⁻¹ at 1000 mA g ⁻¹ after 2000 cycles	23
3D N-HPC	/		345 mA h g ⁻¹ at 0.1 A g ⁻¹ 280 mA h g ⁻¹ at 0.2A g ⁻¹ 223 mA h g ⁻¹ at 0.5 A g ⁻¹ 180 mA h g ⁻¹ at 1 A g ⁻¹ 149mA h g ⁻¹ at 2 A g ⁻¹ 113mA h g ⁻¹ at 5 A g ⁻¹	292 mA h g ⁻¹ after 400 cycles at 0.1 A g ⁻¹ ; 157 mA g ⁻¹ after 12000 cycles at 2.0 Ag ⁻¹ .	24
N-doped C/GO coupled polyhedral microframe	40		374.3 mA h g ⁻¹ at 0.2 A g ⁻¹ 333.9 mA h g ⁻¹ at 0.4A g ⁻¹ 316.8 mA h g ⁻¹ at 0.6 A g ⁻¹ 294.4 mA h g ⁻¹ at 0.8 A g ⁻¹ 272.2mA h g ⁻¹ at 1 A g ⁻¹	358.4 mA h g ⁻¹ after 100 cycles at 0.1 A g ⁻¹ ; 189.5 mA h g ⁻¹ after 1800 cycles at 2 A g ⁻¹ .	25
S/N dual doped hard C	35		276 mA h g ⁻¹ at 0.1 A g ⁻¹ 265 mA h g ⁻¹ at 0.2A g ⁻¹ 245 mA h g ⁻¹ at 0.3 A g ⁻¹ 236 mA h g ⁻¹ at 0.5A g ⁻¹ 224mA h g ⁻¹ at 0.8 A g ⁻¹ 212mA h g ⁻¹ at 1 A g ⁻¹ 199mA h g ⁻¹ at 1.5 A g ⁻¹	234.5 mAh g ⁻¹ after 300 cycles at 0.1 A g ⁻¹ ; 189.3 mAh g ⁻¹ after 400 cycles at 0.5 A g ⁻¹ .	26
3D high edge-N doped turbostratic C	48.7		434 mA h g ⁻¹ at 0.05 A g ⁻¹ 364 mA h g ⁻¹ at 0.1A g ⁻¹ 330 mA h g ⁻¹ at 0.2 A g ⁻¹ 281 mA h g ⁻¹ at 0.5 A g ⁻¹ 246 mA h g ⁻¹ at 1A g ⁻¹ 225 mA h g ⁻¹ at 2 A g ⁻¹ 93 mA h g ⁻¹ at 5A g ⁻¹	353 mAh g ⁻¹ after 800 cycles at 1 A g ⁻¹ .	27
3D N-doped framework C	24.3		309 mA h g ⁻¹ at 0.1A g ⁻¹ 247 mA h g ⁻¹ at 0.2 A g ⁻¹ 198 mA h g ⁻¹ at 0.5 A g ⁻¹ 168 mA h g ⁻¹ at 1A g ⁻¹ 225 mA h g ⁻¹ at 2 A g ⁻¹ 146 mA h g ⁻¹ at 5A g ⁻¹	137 mAh g ⁻¹ after 1000 cycles at 2 A g ⁻¹	28

N/S dual-doped GO	/	192 mA h g ⁻¹ at 1A g ⁻¹ 155 mA h g ⁻¹ at 2 A g ⁻¹ 122 mA h g ⁻¹ at 5A g ⁻¹ 97.2 mA h g ⁻¹ at 10A g ⁻¹ 91.4 mA h g ⁻¹ at 2 0A g ⁻¹	220 mAh g ⁻¹ after 1200 cycles at 0.5 A g ⁻¹ . 100 mAh g ⁻¹ after 5000 cycles at 5 A g ⁻¹	29
N/O dual-doped C nanospheres	29.3	341 mA h g ⁻¹ at 0.05 A g ⁻¹ 311 mA h g ⁻¹ at 0.1A g ⁻¹ 330 mA h g ⁻¹ at 0.2 A g ⁻¹ 295 mA h g ⁻¹ at 0.5 A g ⁻¹ 246 mA h g ⁻¹ at 1A g ⁻¹ 225 mA h g ⁻¹ at 2 A g ⁻¹ 193 mA h g ⁻¹ at 3A g ⁻¹ 111 mA h g ⁻¹ at 5A g ⁻¹	346 m h g ⁻¹ after 360 cycles at 0.05 A g ⁻¹ . 243 mA h g ⁻¹ after 2000 cycles at 1A g ⁻¹	30
N-doped CNF	49	238 mA h g ⁻¹ at 0.1A g ⁻¹ 217 mA h g ⁻¹ at 0.2 A g ⁻¹ 192 mA h g ⁻¹ at 0.5 A g ⁻¹ 172 mA h g ⁻¹ at 1A g ⁻¹ 153 mA h g ⁻¹ at 2A g ⁻¹ 126 mA h g ⁻¹ at 5A g ⁻¹	248 mAh g ⁻¹ after 100 cycles at 0.025 A g ⁻¹ . 146 mAh g ⁻¹ after 2000 cycles at 2 A g ⁻¹ .	31
O-Sb-N SA@NC	62	638 mA h g⁻¹ at 0.05 A g⁻¹ 576 mA h g⁻¹ at 0.1A g⁻¹ 576 mA h g⁻¹ at 0.2 A g⁻¹ 312 mA h g⁻¹ at 0.5 A g⁻¹ 238 mA h g⁻¹ at 1A g⁻¹ 225 mA h g⁻¹ at 2 A g⁻¹ 166 mA h g⁻¹ at 4A g⁻¹	593.3 mAh g⁻¹ after 100 cycles at 0.1 A g⁻¹. 194.5 mAh g⁻¹ after 2000 cycles at 2A g⁻¹	This work

Table S5. The comparison of the cycling performance of the full cell in our work with previously reported of full PIBs.

Full cell Anode//cathode	Cycling performance	Capacity retention	Ref.
Soft-C// KFeC ₂ O ₄ F	76.2 mAh g ⁻¹ after 200 cycles at 0.1A g ⁻¹	90%	32
RPCNS-800//PTCDA	19 mAh g ⁻¹ at 5 A g ⁻¹ after 5000 cycles	59.5%	33
GO// KNiHCF	87.1 mA h g ⁻¹ after 500 cycles at 0.1 A g ⁻¹ .	87.1%	34
MCS//PTCDA	66.4 mA h g ⁻¹ after 200 cycles at 1 A g ⁻¹ .	56.8%	35
Cs@MoSSe@C// KFeHCF	87.1 mA h g ⁻¹ after 100 cycles at 1 A g ⁻¹ .	87.1%	36
C@GO//KPB	67.5 mA h g ⁻¹ after120 cycles at 0.05 A g ⁻¹ .	84.5%	25
Co _{0.85} Se@N-C// K _{0.5} MnO ₂	65 mA h g ⁻¹ after50 cycles at 0.05 A g ⁻¹ .	65%	37
EGO//NOCNB	85 mA h g ⁻¹ after 200 cycles at 0.1 A g ⁻¹ .	94%	22
NCNF-650//KPB	190 mA h g ⁻¹ after 30 cycles at 0.2 A g ⁻¹ .	91%	31
SnS ₂ @C-2//KPB	82.5 mA h g-1 after 30 cycles at 0.1 A g-1.	88.7%	38
Bulk Sb//K _x CrO ₂	67 mA h g ⁻¹ after 100 cycles at 0.1 A g ⁻¹	80%	39
PNCM//PTCDA	113 mA h g-1 after 70 cycles at 0.1 A g-1	36.8%	40
WFe _{x-1} Se _x @MFCR//KVP	137.8 mA h g-1 after 400 cycles at 0.1 A g ⁻¹	~84%	41
CoSe@NCNTs//KPB	228 mA h g-1 after 200 cycles at 0.5 A g ⁻¹	~66%	42
Super P//KMO-H	29.2 mA h g-1 after 50 cycles at 0.1 A g-1	64.3%	43
Bi@NC-800//KPB	~59 mA h g ⁻¹ after 100 cycles at 2.5C	87.3%	44
Sb//KPB	508 mA h g-1 after 50 cycles at 0.2 A g ⁻¹	98.2%	19
O-Sb-N SA@NC// KFeHCF	67 mAh g⁻¹ after 1200 cycles at 5A g⁻¹	98.7% (100 cycles in 5A g⁻¹) 88.9% (500 cycles in 5A g⁻¹) 81% (1200 cycles in 5A g⁻¹)	This work

References

1. G. Kresse and J. Hafner, *Phys Rev B Condens Matter*, 1993, **47**, 558–561.
2. G. Kresse and J. Hafner, *Phys Rev B Condens Matter*, 1994, **49**, 14251–14269.
3. G. Kresse, *PhysRevB*, 1996, **54**, 54.
4. P. E. Blochl, *Phys Rev B Condens Matter*, 1994, **50**, 17953–17979.
5. K. G and F. J, *Comput. Mater. Sci*, 1996, **6**, 15–50
6. K. B. John P. Perdew, Matthias Ernzerhof, *Phy. Rev. Lett*, 1996, **77**, 3865.
7. J. Behler, *J Chem Phys*, 2011, **134**, 074106.
8. J. Cui, H. Zheng, Z. Zhang, S. Hwang, X.-Q. Yang and K. He, *Matter*, 2021, **4**, 1335–1351.
9. J. Li, W. Qin, J. Xie, H. Lei, Y. Zhu, W. Huang, X. Xu, Z. Zhao and W. Mai, *Nano Energy*, 2018, **53**, 415–424.
10. Q. Zhang, B. Han, Y. Zou, S. Shen, M. Li, X. Lu, M. Wang, Z. Guo, J. Yao, Z. Chang and M. Gu, *Adv. Mater.*, 2021, **33**, e2102666.
11. W. Zhang, J. Yin, M. Sun, W. Wang, C. Chen, M. Altunkaya, A. H. Emwas, Y. Han, U. Schwingenschlogl and H. N. Alshareef, *Adv. Mater.*, 2020, **32**, e2000732.
12. Y. Chen, B. Xi, M. Huang, L. Shi, S. Huang, N. Guo, D. Li, Z. Ju and S. Xiong, *Adv. Mater.*, 2022, **34**, e2108621.
13. S. Dou, J. Xu, C. Yang, W.-D. Liu, I. Manke, W. Zhou, X. Peng, C. Sun, K. Zhao, Z. Yan, Y. Xu, Q. Yuan, Y. Chen and R. Chen, *Nano Energy*, 2022, **93**, 106903.
14. R. C. Cui, B. Xu, H. J. Dong, C. C. Yang and Q. Jiang, *Adv. Sci.*, 2020, **7**, 1902547.
15. L. Tao, Y. Yang, H. Wang, Y. Zheng, H. Hao, W. Song, J. Shi, M. Huang and D. Mitlin, *Energy Storage Mater.*, 2020, **27**, 212–225.
16. H. Wang, X. Wu, X. Qi, W. Zhao and Z. Ju, *Mater. Res. Bull.*, 2018, **103**, 32–37.
17. X. Hu, G. Zhong, J. Li, Y. Liu, J. Yuan, J. Chen, H. Zhan and Z. Wen, *Energy Environ. Sci.*, 2020, **13**, 2431–2440.
18. Y. An, Y. Tian, L. Ci, S. Xiong, J. Feng and Y. Qian, *ACS Nano*, 2018, **12**, 12932–12940.
19. X.-D. He, Z.-H. Liu, J.-Y. Liao, X. Ding, Q. Hu, L.-N. Xiao, S. Wang and C.-H. Chen, *J. Mater. Chem. A*, 2019, **7**, 9629–9637.
20. J. Ruan, Y. Zhao, S. Luo, T. Yuan, J. Yang, D. Sun and S. Zheng, *Energy Storage Mater.*, 2019, **23**, 46–54.
21. H. Ding, J. Wang, L. Fan, Z. Liu, X. Jia, X. Yu and B. Lu, *Chem. Eng. J.*, 2020, **395**, 125147.
22. K. Zhang, Q. He, F. Xiong, J. Zhou, Y. Zhao, L. Mai and L. Zhang, *Nano Energy*, 2020, **77**, 105018.
23. W. Yang, J. Zhou, S. Wang, Z. Wang, F. Lv, W. Zhang, W. Zhang, Q. Sun and S. Guo, *ACS Energy Lett.*, 2020, **5**, 1653–1661.
24. X. Zhou, L. Chen, W. Zhang, J. Wang, Z. Liu, S. Zeng, R. Xu, Y. Wu, S. Ye, Y. Feng, X. Cheng, Z. Peng, X. Li and Y. Yu, *Nano Lett.*, 2019, **19**, 4965–4973.
25. B. Wang, F. Yuan, Q. Yu, W. Li, H. Sun, L. Zhang, D. Zhang, Q. Wang, F. Lai and W. Wang, *Energy Storage Mater.*, 2021, **38**, 329–337.
26. Y. Liu, H. Dai, L. Wu, W. Zhou, L. He, W. Wang, W. Yan, Q. Huang, L. Fu and Y.

- Wu, *Adv. Energy Mater.*, 2019, **9**, 1901379.
27. W. Zhang, M. Sun, J. Yin, W. Wang, G. Huang, X. Qiu, U. Schwingenschlögl and H. N. Alshareef, *Nano Energy*, 2021, **87**, 106184.
 28. B. Yang, J. Chen, L. Liu, P. Ma, B. Liu, J. Lang, Y. Tang and X. Yan, *Energy Storage Mater.*, 2019, **23**, 522–529.
 29. C. Lu, Z. Sun, L. Yu, X. Lian, Y. Yi, J. Li, Z. Liu, S. Dou and J. Sun, *Adv. Energy Mater.*, 2020, **10**, 2001161.
 30. H. Deng, L. Wang, S. Li, M. Zhang, T. Wang, J. Zhou, M. Chen, S. Chen, J. Cao, Q. Zhang, J. Zhu and B. Lu, *Adv. Funct. Mater.*, 2021, **31**, 2107246.
 31. Y. Xu, C. Zhang, M. Zhou, Q. Fu, C. Zhao, M. Wu and Y. Lei, *Nat. Commun.*, 2018, **9**, 1720.
 32. B. Ji, W. Yao, Y. Zheng, P. Kidkhunthod, X. Zhou, S. Tunmee, S. Sattayaporn, H.-M. Cheng, H. He and Y. Tang, *Nat. Commun.*, 2020, **11**, 1225.
 33. H. Deng, L. Wang, S. Li, M. Zhang, T. Wang, J. Zhou, M. Chen, S. Chen, J. Cao, Q. Zhang, J. Zhu and B. Lu, *Adv. Funct. Mater.*, 2021, **31**, 2107246.
 34. L. Li, Z. Hu, Y. Lu, C. Wang, Q. Zhang, S. Zhao, J. Peng, K. Zhang, S.-L. Chou and J. Chen, *Angewandte Chemie International Edition*, 2021, **60**, 13050–13056.
 35. J. Zheng, Y. Wu, Y. Tong, X. Liu, Y. Sun, H. Li and L. Niu, *Nano-Micro Lett.*, 2021, **13**, 174.
 36. M. Cai, H. Zhang, Y. Zhang, B. Xiao, L. Wang, M. Li, Y. Wu, B. Sa, H. Liao, L. Zhang, S. Chen, D.-L. Peng, M.-S. Wang and Q. Zhang, *Sci. Bull.*, 2022, **67**, 933–945.
 37. G. Ma, C. Li, F. Liu, M. K. Majeed, Z. Feng, Y. Cui, J. Yang and Y. Qian, *Mater. Today Energy*, 2018, **10**, 241–248.
 38. D. Li, L. Dai, X. Ren, F. Ji, Q. Sun, Y. Zhang and L. Ci, *Energy Environ. Sci.*, 2021, **14**, 424–436.
 39. L. Zhou, Z. Cao, J. Zhang, H. Cheng, G. Liu, G.-T. Park, L. Cavallo, L. Wang, H. N. Alshareef, Y.-K. Sun and J. Ming, *Adv. Mater.*, 2021, **33**, 2005993.
 40. Y. Xie, Y. Chen, L. Liu, P. Tao, M. Fan, N. Xu, X. Shen and C. Yan, *Adv. Mater.*, 2017, **29**, 1702268.
 41. J. Cao, L. Wang, D. Li, Z. Yuan, H. Xu, J. Li, R. Chen, V. Shulga, G. Shen and W. Han, *Adv. Mater.*, 2021, **33**, 2101535.
 42. Y. Liu, Q. Deng, Y. Li, Y. Li, W. Zhong, J. Hu, X. Ji, C. Yang, Z. Lin and K. Huang, *ACS Nano*, 2021, **15**, 1121–1132.
 43. S. Chong, Y. Wu, Y. Chen, S. Guo, Z. Tai, C. Shu, Q. Tan, J. Sun and Y. Liu, *Electrochim. Acta*, 2019, **293**, 299–306.
 44. X. Xiang, D. Liu, X. Zhu, Y. Wang, D. Qu, Z. Xie, X. Zhang and H. Zheng, *ACS Appl. Mater. Interfaces*, 2022, **14**, 34722–34732.